A Simple and Efficient Quasi-3D Magnetic Equivalent Circuit for Surface Axial Flux Permanent Magnet Synchronous Machines

Ahmed Hemeida, Antti Lehikoinen, Paavo Rasilo, Hendrik Vansompel, Anouar Belahcen, Antero Arkkio, and Peter Sergeant

***Abstract*—This paper presents a simple and efficient magnetic equivalent circuit (MEC) model for surface axial flux permanent magnet synchronous machines. The MEC model is used to solve all the electromagnetic properties of the machine including the no load, full load voltages, cogging torque, torque ripple and stator iron core losses. Moreover, this approach can be extended for all surface permanent magnet synchronous machines. The main novelty of this approach is the development of a static system, which accounts for the rotation. The model takes into account the rotor rotation via time dependent permanent magnet magnetization sources. The static system matrix facilitates a very fast solving. In addition, to take into account the 3D effect, a multi-slicing of the machine in the radial direction is done. This boosts the simulation time to only 60 seconds for 6 slices and 50 time steps including the non-linear behaviour of the stator elements with a great accuracy. Additionally, the number of elements in the MEC can be adjusted to reduce the computational time. This model is verified by means of 3D and 2D multi slice finite element (FE) models. In addition, experimental validations are also provided at the end.**

***Index Terms*—Analytical modeling, Axial flux permanent magnet synchronous machines (AFPMSM), Cogging torque, Magnetic equivalent circuit (MEC), Surface permanent magnet synchronous machines (SPMSM), Torque ripple.**

I. Introduction

AXIAL flux permanent magnet synchronous machines (AFPMSM) have been the subject of significant, worldwide research efforts for the past 20 years and can now be considered as a mature technology. Different AFPMSM concepts with different topologies are described in Figs. 1 (a), (b), (c) and (d) [1]. These machines are (a) the yokeless and segmented armature (YASA) machine, (b) the axial flux machine with internal rotor (AFIR), (c) and (d) the toroidally wound machine with internal stator, in two variants.

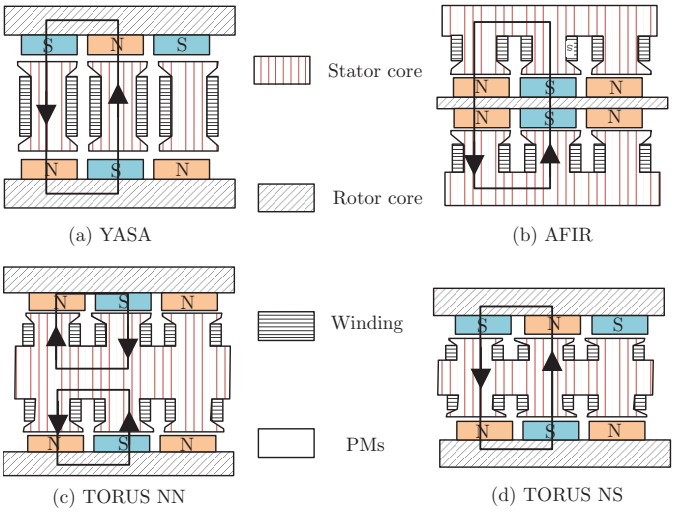

Fig. 1. Schematic representation of different configurations of the AFPMSM [1].

Accurate and fast modeling techniques are indispensable for a complete design of electric machines. A multi-physical design is mandatory *i.e.* for involving thermal, electromagnetic, and mechanical modeling. This paper focuses on the electromagnetic modeling of the surface permanent magnet (PM) machines. The yokeless and segmented armature (YASA) machine is selected as an application for this study.

Several numerical and analytical techniques were developed and used over last decades [2]–[4]. Although numerical techniques, such as 3D and 2D finite element (FE) analysis [5]–[7], are the most accurate techniques to model electric machines, they are not preferable in early design stages due to their expensive computational burden.

Therefore, in the predesign, analytical tools are used to predict the electromagnetic parameters. Generally speaking, analytical tools can be classified into three main categories

Manuscript received February 21, 2018; revised April 14, 2018, July 2,1028, and September 17, 2018; accepted November 09, 2018. This research was partly supported by the European Research Council (ERC) within the European Unions Seventh Framework Programme (FP7/2007-2013)/ERC under Grant 339380.

Ahmed Hemeida, Antti Lehikoinen, Paavo Rasilo, Anour Belahcen, and Antero Arkkio are with the Department of Electrical Engineering and Automation, Aalto University, Espoo, P.O. Box 15500, FI-00076, Finland (e-mail: a.hemeida@ieee.org, antti.lehikoinen@aalto.fi, paavo.rasilo@tut.fi, anouar.belahcen@aalto.fi, antero.arkkio@aalto.fi).

Ahmed Hemeida is also with Electrical Power and Engineering Department, Cairo University, 12613, Cairo, Egypt.

Paavo Rasilo is also with Tampere University of Technology, Laboratory of Electrical Energy Engineering, P.O. Box 692, FI-33101 Tampere, Finland.

Hendrik Vansompel and Peter Sergeant are with the Electrical Energy Laboratory, Department of Electrical Energy, Metals, Mechanical Constructions and Systems, Ghent University, 9000 Ghent, Belgium, and also with Flanders Make, the strategic research centre for the manufactur-ing industry, 3920 Lommel, Belgium (e-mail: Hendrik.Vansompel@UGent.be, Peter.Sergeant@UGent.be).

[8], [9] for surface PMSMs. The authors in [8], [9] compared mainly between (1- the magnetic equivalent circuit (MEC) model), (2- the Fourier based models), and (3- a combined solution of MEC and Fourier based models.) The criteria of the selection are based on the simulation time, capability to calculate mean torque, induced voltage, torque ripple and cogging torque.

The MEC model is based on representing the electric machine with a magnetic reluctance network that depends on machine geometrical parameters and non-linear magnetic material properties. In such a technique, the modeling accuracy highly depends on the used discretization level. Additionally, it is important to model the air gap by reasonable reluctance paths, that change continuously with the rotation of the electric machines. This means that at each rotor position, all rotor and stator nodes need to be aligned with the air gap nodes [10], [11], which increases the complexity of the MEC.

In [12], the MEC was developed for an interior radial flux fractional slot permanent magnet synchronous machine. Although a huge reluctance network size was utilized, cogging torque and torque ripple results were not validated.

In order to simplify the air gap reluctance representation, the alignment between the rotor and stator is divided into three states in [10]; a state when a little part of the magnet contributes to the MMF in the stator, a state when a higher part contributes and a state when it totally contributes. However, a very large matrix is obtained and the problem becomes more complex. Additionally, this method does not ensure accurate computation of the cogging torque and torque ripple.

Other attempts have been made to simplify the air gap reluctance representation, such as the refined mesh approach, that was proposed in [11]. In the refined mesh approach, each magnet is subdivided into a high number of elements, *i.e.* 15, which allows the demagnetization effect investigation. The reluctances connecting a stator tooth and a rotor element are obtained by integrating the product of their window functions and the inverse of the air gap length function. Although the MEC accuracy is highly improved using this refined mesh approach, the complexity dramatically increases. This model is capable to predict all electromagnetic parameters. However, with respect to complexity and computational time, the model is not efficient.

When AFPMSM are being modeled using the MEC model, the machine is divided into a number of radial slices, where the magnetic equivalent model is applied in each slice [13].In [13], the developed MEC model of the AFPMSM was nicely validated with FE model, but only for the mean value of the torque and the terminal voltage. The cogging torque and torque ripple were not computed.

It is clear that there are some difficulties in the existing MEC model regarding the connection between stator and rotor reluctances. Each time the rotor rotates, the reluctances need to be aligned again. Additionally, one needs very high discretization to obtain the cogging torque and torque ripple and hence the complexity increases.

A second approach is to use the Fourier based models. These models can nicely predict the air gap flux density and therefore predict the cogging torque and torque ripple efficiently. A comparative study between different concepts of Fourier based subdomain (SD) models and conformal mapping techniques for AFPMSM and radial flux permanent magnet synchronous machines (RFPMSMs) has been presented in [7], [14] respectively. For the calculation of the no load voltages, the result is satisfactory for all models. However, for torque ripple and cogging torque calculation, the SD model is the most accurate technique to predict them. These SD models assume infinite permeability for the stator and rotor iron cores.

New pure Fourier based models that include saturation in the iron core were presented in [15]. In addition, a hybrid Fourier based model and a MEC model was presented in [16]. This model is based on solving the Poisson equations firstly assuming infinite permeability and imposing the solution to the MEC model afterwards. In [17], the authors compared between a hybrid Fourier based model and a conventional reluctance network. The hybrid model is based on modeling the rotor, the permanent magnets (PMs) and the air gap region by a Fourier based model and the stator by a reluctance network. The strong coupling between both models is done by equalizing the magnetic scalar potential on the interface region between the stator and air gap area. They concluded that the hybrid method gives better performance in terms of CPU time.

In all the aforementioned analytical models, the 2D multi-slicing modeling technique is used. The authors in [16] compared between the 2D multi-slicing modeling technique and the 3D FE model. Additionally, they obtained the optimum number of slices for different permanent magnet PM shapes.

Moreover, the authors in [2], [18] carried out a parametric study to analyze the end effects on the accuracy of the multi-slicing modeling technique compared to the 3D FE model. It is demonstrated that the multi-slicing technique can be advantageously used for design purposes.

To obtain the benefits from the ability to model the non-linear behaviour of the material in the traditional MEC model and the ability to compute the cogging torque and torque ripple from the Fourier based models, a simple and an efficient model is developed to tackle this.

In this article, instead of rotating the reluctance between the rotor and the stator, the magnetization sources are rotated. Therefore, the system matrix has to be created only once. For all consecutive time steps, only a multiplication is required of the inverted matrix with the time dependent source vector. Therefore, the MEC model can be used to predict all the electromagnetic parameters of the machine including voltages, mean torque, torque ripple and cogging torque.

II. Modeling Principle

In the 3D and 2D multi-slice FE models, described in Figs. 2 (a) and (c) respectively, only half of the machine is modeled and a symmetry boundary condition is imposed at half of the tooth.

The idea of the multi-slice 2D FE model is to stretch the machine over the radial length of the machine to n_{s} slices [16]. Each slice has an average radius of R^i_{av} and a radial length t_{cp}. The 3D to 2D transformation is shown in Fig. 2 (b). In all the 2D FE models, the radial component of the magnetic

flux density is neglected. Each slice represents a 2D FE model shown in Fig. 2 (c). The axis definition in Fig. 2 (b) is R for the radial direction, and $\theta_{\rm m}$ for circumferential direction. The x, y-axes in Fig. 2 (c) present the circumferential and axial direction.

The 3D and 2D multi-slice FE models are used as the reference solution to evaluate the accuracy of MEC model. Comsol software is used to conduct the FE simulations. The novelty of the MEC model is illustrated in next subsection.

A. Operation Principle

The MEC is based on the representation of the major flux sources and lumped reluctance elements. The flux sources are the magneto-motive force (MMF) sources, which represent the injected electric currents in the windings. On the other hand, the PM is usually modeled by a magneto-motive force in series to a self reluctance. The lumped reluctance elements consist of linear and non-linear reluctances of the stator and rotor cores. They are dependent on the relative permeability of the used material. The stator core relative permeability is a function of the flux passing through the element itself. The PM and air gap permeability in this case are constant.

The MEC model is solved in a similar way to the 2D FE model described in Fig. 2 (c). The machine is stretched at different slices i in the radial direction R described in Fig. 2 (b). Each slice i has an average radius $R^i_{\rm av}$ and radial length $t_{\rm cp}$.

It is possible to obtain any quantity like torque, induce voltage, *etc.* by summation of all slices values.

As previously outlined, a novel approach is proposed to avoid the alignment between the rotor and stator reluctances. In this technique, regardless of the rotating rotor, the PMs are assumed to have varying flux sources that are rotating in space according to the angle of rotation. Accordingly, the reluctances of these PMs are constant.

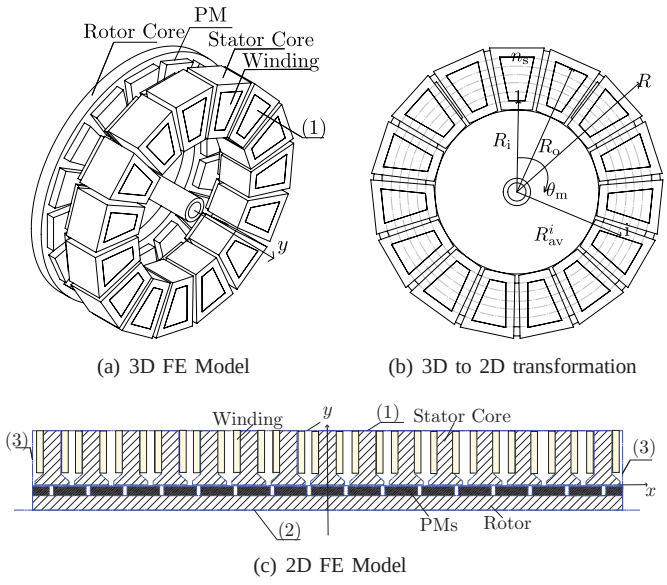

(a) 3D FE Model (b) 3D to 2D transformation

(c) 2D FE Model

Fig. 2. 3D and 2D FE models. (1) Neumann boundary condition. (2) Dirichlet boundary condition. (3) Periodic boundary condition [19].

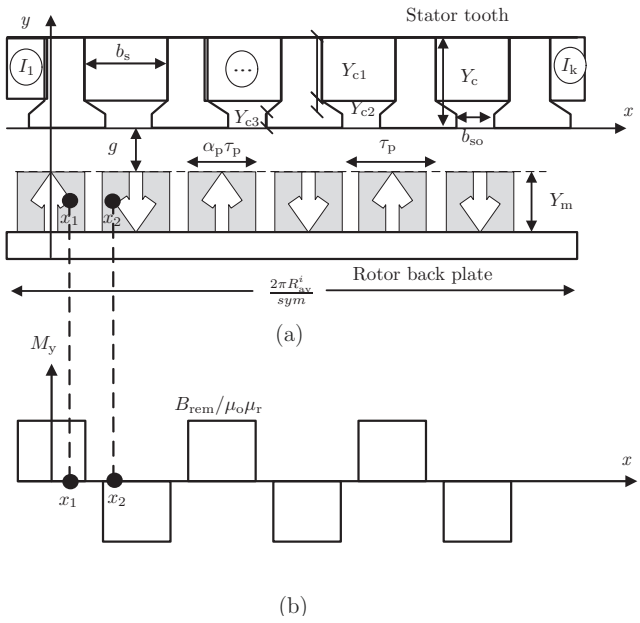

Fig. 3. MEC model at a radial slice number i with the PM magnetization. (a) AFPMSM geometry. (b) PM magnetization.

Therefore, the PMs are modeled by equivalent Fourier based sources that are shown in Fig. 3 (a) and (b). Fig. 3 (a) shows the i stretched slice with all geometrical quantities of tooth axial length ($Y_{\rm c}$, $Y_{\rm c1}$, $Y_{\rm c2}$, $Y_{\rm c3}$), slot width $b_{\rm s}$, slot opening $b_{\rm so}$, air gap length g, PM axial length $Y_{\rm m}$, PM pole pitch $\tau_{\rm p}$, and the PM pole arc ratio $\alpha_{\rm p}$. The currents are described by I_1 in different slot regions.

Assuming one PM with a remanent magnetic flux density of ($B_{\rm m}$) is operating with a negative field intensity of (-$H_{\rm m}$ and a total magnetic flux density of ($B_{\rm m}$). The constitutive relation in one PM can be described as:

$$B_{\rm m} = B_{\rm rem} - \mu_{\rm o}\mu_{\rm r}H_{\rm m}. \tag{1}$$

The relationship described in (1) is extended to the entire PM region. Therefore, it becomes function of the time t and the circumferential distance $x = R^i_{\rm av}\theta_{\rm m}$. It converts to:

$$B_{\rm m}(x,t) = \mu_{\rm o}\mu_{\rm r}M_{\rm y}(x,t) - \mu_{\rm o}\mu_{\rm r}H_{\rm m}(x,t). \tag{2}$$

where $M_{\rm y}(x,t)$ is the Fourier-series expansion of the magnetization vector shown in Fig. 3 (b) at any time instant t as a function of the circumferential distance $x = R^i_{\rm av}\theta_{\rm m}$ and can be obtained as [16]:

$$M_{\rm y}(x,t) = \sum_{n=1,3,5,\ldots}^{\infty} M_{\rm n_i}\cos\left(\frac{n\pi\left(x - R^i_{\rm av}\int\Omega_{\rm m}(t)\,{\rm d}t\right)}{\tau_{\rm p_i}}\right), \tag{3}$$

where n is the harmonic order, $\Omega_{\rm m}$ is the mechanical speed in rad/s, $\tau_{\rm p_i}$ is the pole pitch at a slice number i. The number of harmonic orders taken in the simulations are 50. The amplitudes of the fourier series expansion are described as:

$$M_{\rm n_i} = \frac{4B_{\rm rem}}{n\pi\mu_{\rm o}\mu_{\rm r}}\sin\left(\frac{n\pi\alpha_{\rm p_i}}{2}\right), \tag{4}$$

where α_{p_i} is the PM angle ratio of PM width to the pole pitch, $B_{\rm rem}$ is the remanent PM flux density, $\mu_{\rm o}$ is the free air permeability, and $\mu_{\rm r}$ is the relative permeability of the PM which equals 1.05.

In the developed MEC, the tooth is discretized to many nodes. In each node, it is required to input a value for the magnetomotive force $F_{\rm pm}$ in the PM region. Therefore, the average value of the MMF can be used.

Let us assume two points x_1 and x_2, shown in Fig. 3 (b), in the space in the PM region. x_1 exists in the north PM as shown in Fig. 3 (b). x_2 exists in the south PM region. If larger portion between the two points exists in one of the PMs, the average MMF is not zero. Therefore, integration between the two points is done to obtain the average MMF.

The MMF at any point x_1 in the space in the PM region can be obtained by multiplying the magnetization vector (3) at a point x_1 and a certain time instant t by the axial length of the PMs $Y_{\rm m}$:

$$F_{\rm pm_1} = Y_{\rm m} M_{\rm y}(x_1, t). \tag{5}$$

To obtain the average MMF between the two points x_1 and x_2, shown in Fig. 3 (b), integration of (5) between the two points x_1 and x_2 is done. The output is divided by the length between the two points $(x_2 - x_1)$. This is given by:

For each time step, the result of the integration in (6) is used as sources for the MEC. In next subsection, the principle of MEC operation is illustrated.

$$\begin{aligned} F_{\rm pm_{2,1}} &= \frac{Y_{\rm m}}{x_2 - x_1} \int_{x_1}^{x_2} M_{\rm y}(x,t) {\rm d}x \\ &= \frac{Y_{\rm m}}{x_2 - x_1} \sum_{n=1,3,5,\ldots}^{\infty} \frac{\tau_{\rm p_i}}{n\pi} M_{\rm n_i} \\ &\left[\sin\left(\frac{n\pi\,(x_2 + x_{\rm s})}{\tau_{\rm p_i}} \right) - \sin\left(\frac{n\pi\,(x_1 + x_{\rm s})}{\tau_{\rm p_i}} \right) \right]. \end{aligned} \tag{6}$$

However, it is possible to present the PMs as rectangular shape as presented in Fig. 3 (b). Afterwards, it is possible to rotate the PMs in space for each rotor position according to the time instant. A numerical integration could be done at the end to obtain the average MMF between the two points x_1 and x_2 for this rectangular function.

B. Sub-Division Principle

The MEC is programmed so as to allow the choice of the number of divisions. Fig. 4 shows one tooth with the corresponding area of the PMs and the rotor.

Each tooth in the machine is divided in the circumferential direction to $2n_{\rm x1}+2n_{\rm x2}+n_{\rm x3}$ elements. In the axial direction, the number of elements are $n_{\rm y1}+n_{\rm y2}+n_{\rm y3}+n_{\rm y4}+n_{\rm y5}+n_{\rm y6}$. Fig. 4 shows the case with minimal refinement *i.e.* $n_{\rm x1} = n_{\rm x2} = n_{\rm x3} = \cdots = 1$.

There are two different sources in the circuit as described in Fig. 4. The currents imposed in the winding can be represented by a magnetomotive force $F_{\rm c}$. The PMs can be modeled by (6). The value of (6) should be divided by the number of divisions in the PMs region $n_{\rm y5}$. As described before, the solution is obtained for different slices and the total solution is then obtained.

C. Matrices Assembly

In this part, the matrix assembly is demonstrated. The mesh based MEC configuration is used in this article. It is proved that this type of solution gives faster result than the nodal based configuration [20].

In this article, the number of loops and branches are $n_{\rm l}$ and $n_{\rm b}$ respectively [21]. The vector $\mathbf{\Phi}$ depicts the flux in each loop. The size of $\mathbf{\Phi}$ is $[n_{\rm l} \times 1]$. It can be determined by [21]:

$$\mathbf{r} = \mathbf{L}^{\mathbf{T}} \left(\mathbf{R}_{\rm air} + \mathbf{R}_{\rm iron} \bullet \nu_{\rm r} \right) \mathbf{L}\mathbf{\Phi} - (\mathbf{F}_{\rm c} + \mathbf{F}_{\rm pm}), \tag{7}$$

where $\mathbf{r}$ is the residual function. $\mathbf{L}$ is a loop matrix determining the relation between each branch and the loops associated with it. The size of $\mathbf{L}$ is $[n_{\rm b} \times n_{\rm l}]$. $\mathbf{R}_{\rm air}$, $\mathbf{R}_{\rm iron}$ are the diagonal air and iron reluctance matrices describing the reluctance values at each branch without considering the relative permeability part. The sizes of $\mathbf{R}_{\rm air}$, $\mathbf{R}_{\rm iron}$ are $[n_{\rm b} \times n_{\rm b}]$. $\nu_{\rm r}$ is the relative reluctivity matrix associated with each reluctance in the iron reluctance matrix $\mathbf{R}_{\rm iron}$. It has the same dimension as $\mathbf{R}_{\rm iron}$. $\mathbf{R}_{\rm iron} \bullet \nu_{\rm r}$ is an element-wise product of the iron reluctance and reluctivity matrices. $\mathbf{F}_{\rm c}$, and $\mathbf{F}_{\rm pm}$ are the magnetomotive force (MMF) vectors for the currents and the PMs respectively existing in each loop. All matrices are handled as sparse matrices. This saves lots of memory and calculation times.

The loop matrix $\mathbf{L}$ entries are based on the direction of the loop flux corresponding to the branch flux. This can be illustrated as follows:

$$L_{\rm i,j} = \begin{cases} 1 & \text{loop } j \text{ goes forward in branch } i \\ -1 & \text{loop } j \text{ goes backward in branch } i \\ 0 & \text{otherwise} \end{cases}. \tag{8}$$

The non-linear solution can be solved using Newton-Raphson technique. The loop flux $\mathbf{\Phi}$ in (7) at iteration $k+1$ can be obtained as:

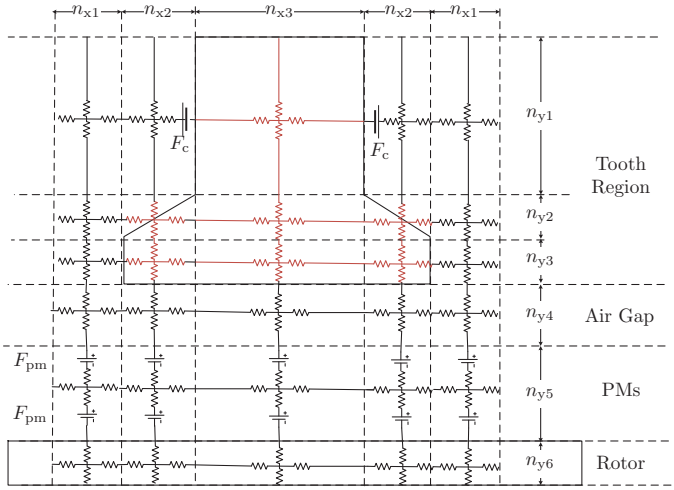

Fig. 4. MEC sub-division principle.

$$\mathbf{\Phi}^{k+1} = \mathbf{\Phi}^{k} - \mathbf{J}(\mathbf{\Phi}^{k})^{-1}\mathbf{r}(\mathbf{\Phi}^{k}), \tag{9}$$

where $\mathbf{\Phi^k}$ is the loop flux at iteration k. $\mathbf{J}(\mathbf{\Phi}^{k})$ is the Jacobian matrix at iteration k. $\mathbf{r}(\mathbf{\Phi}^{k})$ is the residual function at iteration k.

The Jacobian matrix is divided into two parts. One part is the reluctance matrix term $\mathbf{R} = \mathbf{L^T}\left(\mathbf{R}_{\rm air} + \mathbf{R}_{\rm iron} \bullet \nu_{\rm r}\right)\mathbf{L}$. The second one describes the change of the reluctance term with respect to the loop flux. The Jacobian matrix can be described as follows:

$$\mathbf{J} = \mathbf{R} + \mathbf{L^T}\left(\mathbf{R}_{\rm iron} \bullet \mathbf{A}_{\rm area} \bullet \nu_{\rm r_{der}}\right)\Big(\left(\mathbf{L}\mathbf{\Phi}_{\rm d}\mathbf{U}\right) \bullet \mathbf{L}\Big), \tag{10}$$

where $\mathbf{A}_{\rm area}$ is a diagonal matrix of $[n_{\rm b} \times n_{\rm b}]$ elements. Each entry in the $\mathbf{A}_{\rm area}$ is the inverse of the area of each branch in the reluctance element of the iron part. Similarly, $\nu_{\rm r_{der}}$ is a diagonal matrix. Each diagonal entry is the derivative of the relative reluctivity with respect to its associated magnetic flux density and can be described by $\nu_{{\rm der}_{ii}} = \frac{\partial \nu_{ii}}{\partial B_{ii}}$. $\mathbf{\Phi}_{\rm d}$ is a diagonal matrix of the loop flux in each loop $\mathbf{\Phi}$. $\mathbf{U}$ is a $[n_{\rm l} \times n_{\rm l}]$ matrix describing connections between different loop fluxes. The elements of it can be described as:

$$U_{\rm i,j} = \begin{cases} 1 & \text{If } i = j \\ 1 & \text{If } \Phi_{\rm ii} - \Phi_{\rm jj} = \Phi_{\rm b} \text{ (branch flux)} \\ 0 & \text{otherwise} \end{cases}. \tag{11}$$

The Jacobian matrix can be calculated easily without the need to use any for loops in MATLAB. The norm of the percentage error in the flux loops vector is set to 10^{-5}. An example illustrating the use of (7)-(11) is provided in the appendix.

The single valued non-linear constitutive relation of the soft magnetic material is modelled by three material dependent parameters H_0, B_0 and $N_{\rm u}$ [22].

The expression for the relative magnetic reluctivity of the soft magnetic material $\nu_{\rm r}$ as a function of the magnetic flux density B is given by:

$$\nu_{\rm r}(B) = \frac{H_{\rm o}\mu_{\rm o}\left(1 + \left(\frac{B}{B_{\rm o}}\right)^{N_{\rm u}-1}\right)}{B_{\rm o}}, \tag{12}$$

where $\mu_{\rm o}$ is the free space permeability. The material used in the simulations in both the FE and the MEC models is M600-50A. The fitted parameters H_0, B_0 and $N_{\rm u}$ are 237.5A/m, 1.458T, and 20.18.

The $B-H$ curve is shown in Fig. 5. Machines are normally designed to operate around the knee point. For the material M600-50A, the knee point in the $B-H$ curve exists at almost 1.45T.

To account for the radial slices shown in Fig. 2 (b), all matrices are constructed and placed in the diagonal of a new matrix $\mathbf{D}$. This includes all the matrices described in (7)-(11). The winding MMF vector $\mathbf{F}_{\rm c}$, described in (7), is repeated equivalently for all slices. However, the PM magnetization vector $\mathbf{F}_{\rm pm}$ is calculated for each slice independently according to (6). $\mathbf{D}$ can be written as:

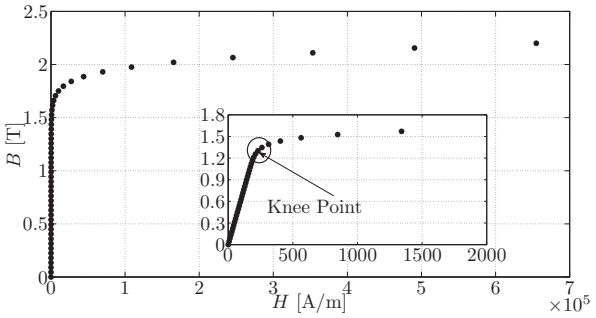

Fig. 5. B-H curve of the M600-50A in the studied models.

$$\mathbf{D} = \begin{bmatrix} \mathbf{D}_1 & \mathbf{0} & \mathbf{0} & \mathbf{0} \\ \mathbf{0} & \ddots & \mathbf{0} & \mathbf{0} \\ \mathbf{0} & \mathbf{0} & \mathbf{D}_{\rm i} & \mathbf{0} \\ \mathbf{0} & \mathbf{0} & \mathbf{0} & \mathbf{D}_{\rm n_s} \end{bmatrix}. \tag{13}$$

The solution of all radial slices can be obtained simultaneously.

To consider the eddy currents effect inside the laminations on the total field distribution, it is possible to account it by presenting the magnetic field strength due to eddy currents as a function of the time derivative of the magnetic flux density as described in [23], [24]. Then the total magnetic field strength can be obtained by summation of both the effects of the non-linear magnetic characteristics and the eddy currents. Afterwards, the total reluctivity is available and can be substituted in (7) and (10) to obtain the residual function $\mathbf{r}$ and the Jaccobian matrix $\mathbf{J}$ respectively.

Skin effect can be accounted for by expressing the flux density distribution in the lamination thickness as a series using a set of skin-effect basis functions as described in [23].

To take into account the effect of end winding on the voltage, an additional term can be added to the voltage equation to express the rate of change of the currents multiplied by the end winding inductances. The end winding inductances formulas can be obtained from [25]. the authors in this article derived a general equation for the concentrated winding.

D. Stator Iron Loss Computation

The flux densities are recorded in all models at different grid points. These flux densities are used to *a posteriori* calculate the iron losses. For the 3D FE model, the three coordinates are recorded to calculate the losses; for the 2D FE model and the MEC model, only the x-y flux densities are recorded. Here, the principle of loss separation is used [26].

The total stator core loss $P_{\rm Fe}$ at each grid point i is recorded. Then a summation of the losses at all grid points n is done to obtain the total losses.

$$P_{\rm Fe} = \sum_{i}^{n}\left\{P_{{\rm hy}_i} + \frac{1}{T}\int_{0}^{T} P_{{\rm cl}_i}(t) + P_{{\rm exc}_i}(t){\rm d}t\right\}. \tag{14}$$

where $P_{{\rm hy}_i}$, $P_{{\rm cl}_i}(t)$, $P_{{\rm exc}_i}(t)$ are the hysteresis, time dependent classical, and time dependent excess losses at each grid point

respectively [26], [27]. The total excess and classical losses are the time averages of the losses over a time period T due to varying flux density B at time instant t. The hysteresis loss depends only on the peak value of the flux density $B_{\mathrm{p_m}}$ at each harmonic order m at a certain grid point. The total hysteresis losses can be obtained by summation of all harmonic orders in the flux density. Each component equals:

$$\begin{aligned} P_{\mathrm{hy_i}} =& k_{\mathrm{Fe},1} B_{\mathrm{p_m}}^{k_{\mathrm{Fe},2}} f \rho V_i, \\ P_{\mathrm{cl_i}}(t) =& k_{\mathrm{Fe},3} \left(\frac{\mathrm{d}B}{\mathrm{d}t}\right)^2 \rho V_i, \\ P_{\mathrm{exc_i}}(t) =& k_{\mathrm{Fe},4} \left(\sqrt{1 + k_{\mathrm{Fe},5} \left|\frac{\mathrm{d}B}{\mathrm{d}t}\right|} - 1\right) \left|\frac{\mathrm{d}B}{\mathrm{d}t}\right| \rho V_i, \end{aligned} \tag{15}$$

where f is the frequency corresponding with the fundamental component. The flux densities used to excite the loss equations in (15) depend on the circumferential and axial components.

$k_{\mathrm{Fe},1}$-$k_{\mathrm{Fe},5}$ are fitting parameters for the losses for the selected iron material. ρ is the iron material density which equals 8760 kg/m^3. The material used in the simulations is M600-50A. The iron losses coefficients $k_{\mathrm{Fe},1}$-$k_{\mathrm{Fe},6}$ of the M600-50 described in (15) are 35.3e-3, 1.7890, 9.264706e-006, 1.875634e-002, 2.093533e-004 respectively.

III. Simulation Results

In order to validate the MEC model, an AFPMSM with 16 poles and 15 tooth coil windings is studied. The geometrical and electromagnetic properties of the machine are described in Table I.

In all subsequent simulations, six radial slices are taken in both the 2D FE model and the MEC model. In the MEC model, the number of discretizations shown in Fig. 4 equal to $n_{\mathrm{x1}} = 8$, $n_{\mathrm{x2}} = 8$, $n_{\mathrm{x3}} = 8$, $n_{\mathrm{y1}} = 3$, $n_{\mathrm{y2}} = 3$, $n_{\mathrm{y3}} = 3$, $n_{\mathrm{y4}} = 3$, $n_{\mathrm{y5}} = 4$, and $n_{\mathrm{y6}} = 3$.

Comsol software is used to conduct the FE simulations. The 3D FE model has a 100000 tetrahedral with a quadratic shape functions. In the 2D FE model, 8000 triangles are used with quadratic shape functions are used to model the machine.

The validation scenario of the MEC model is conducted with respective to different parameters. The comparisons are done with respect to the 3D and 2D multi-slice FE models. This includes the air gap flux densities, the terminal voltage and torque, the cogging torque, the flux density and loss distributions, and the CPU time comparison between different models used. Different loading and geometrical configurations are studied. In addition, a comparison between the traditional MEC and the new MEC is conducted to verify the robustness of the new MEC model.

A. Air Gap Flux Density Comparison

The curves of the MEC and FE models in Figs. 6 and 7 show good correspondence for the normal and circumferential components of the air gap flux densities when loading the machine with the rated current I_{rated}. The total effect of the flux density response on the voltage, torque and cogging torque profiles is illustrated in next subsections for different loading and geometrical conditions.

TABLE I
Geometrical Parameters of the Studied Machine [19].

Parameter	Symbol	Value
Rated power	P_{n}	5 kW
Number of pole pairs	$p = N_{\mathrm{m}}/2$	8
Number of stator slots	N_{s}	15
Rated speed	n_{r}	2500 rpm
Rated torque	T_{em}	19.1 Nm
Outer diameter	D_{o}	148 mm
Inner diameter	D_{i}	100 mm
Axial length core element	$2(Y_{\mathrm{c1}} + Y_{\mathrm{c2}} + Y_{\mathrm{c3}})$	60 mm
Axial length slot	$2Y_{\mathrm{c1}}$	48 mm
Slot width	b_{s}	12 mm
Slot opening width	b_{so}	3 mm

B. Terminal Voltage and Torque Comparisons

The voltage and torque are calculated at no load and rated loading conditions. Fig. 8 shows the phase voltage at no load and rated load conditions. The voltage curves show a good correspondence between the results of the FEs and the MEC model. This figure clearly shows that the MEC model can predict the voltage of the 3D FE model with a maximum percentage of difference of 1.8% for the rated loading condition.

Table II depicts the root mean square (rms) values for the voltage for different loading and geometrical conditions. The errors between both 3D FE, 2D FE model and MEC model are observed. The maximum percentage error between the MEC and the 3D FE model is 1.8%. This proves a great accuracy for the MEC model.

Figure 9 compares different models for torque computations at rated loading condition. This is done using 2D and 3D FE models. The MEC model can track the same shape of the torque of the 2D and 3D FE models.

Table III summarizes the deviation of the mean torque between different models. The torque ripple percentage error is computed with respect to the 3D FE mean torque. The maximum percentage of mean torque error with respect to the 3D model mean torque is 1.1%. The MEC model gives very accurate result for the mean and torque ripple values.

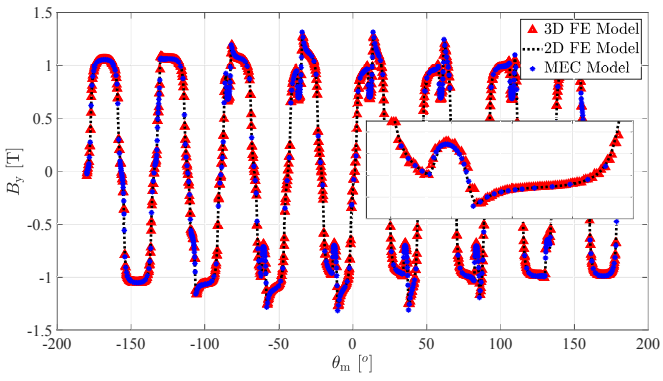

Fig. 6. Axial flux densities comparisons for different models at rated loading condition.

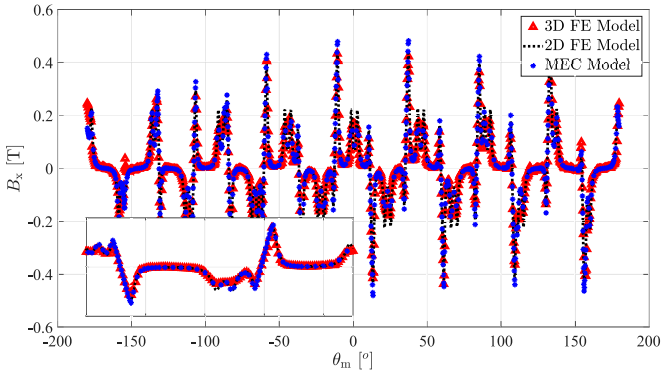

Fig. 7. Circumferential flux densities comparisons for different models at rated loading condition.

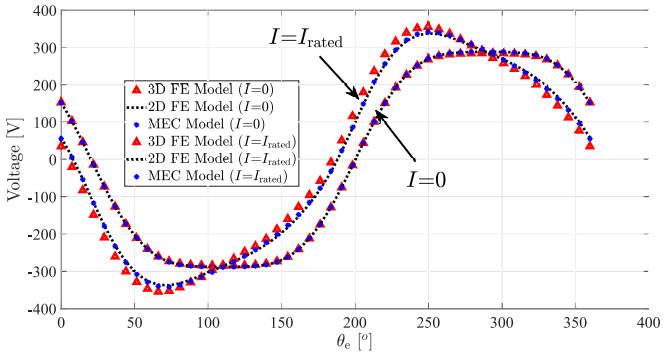

Fig. 8. Voltage waveform for different models at different loading conditions.

C. Cogging Torque Comparison

The 15 poles and 16 slots combination gives very low values of cogging torque because of the high value of the least common multiple of the poles and slots [28]. To make a better presentation for the cogging torque, a machine of 70 poles and 60 slots is used in this subsection only. In this machine, only 1 over 10 of the machine can be simulated. The details of this machine can be found in [7]. This machine has a higher cogging torque amplitude.

Figure 10 shows the difference between the 2D, 3D FE models and the MEC model for cogging torque computation at 5 mm slot opening. The horizontal axis in Fig. 10 indicates the rotor positions while rotating (ϕ_m). It is clear that the MEC model is capable of predicting the cogging torque profile similarly to the FE models.

To ensure the highest accuracy of the MEC model, the slot opening is swapped around certain values. Fig. 11 depicts the peak-to-peak value of the cogging torque as a function of the slot opening over the tooth pitch at minimum radius. The MEC model is very accurate to predict the shape of the peak value for cogging torque for any slot opening.

TABLE II
RMS VALUES FOR THE VOLTAGE FOR DIFFERENT LOADING AND GEOMETRICAL CONDITIONS.

b_{so}	I	Parameter	3D FE Model	2D FE Model	MEC Model
3mm	0	V_{rms} [V]	230	232	232
		$\text{Error}_{V_{\text{rms}}}$ [%]	-	0.9	0.9
	I_{rated}	V_{rms} [V]	247	242	243
		$\text{Error}_{V_{\text{rms}}}$ [%]	-	2	1.6
7mm	0	V_{rms} [V]	221	225	225
		$\text{Error}_{V_{\text{rms}}}$ [%]	-	1.8	1.8
	I_{rated}	V_{rms} [V]	234	231	231
		$\text{Error}_{V_{\text{rms}}}$ [%]	-	1.2	1.2

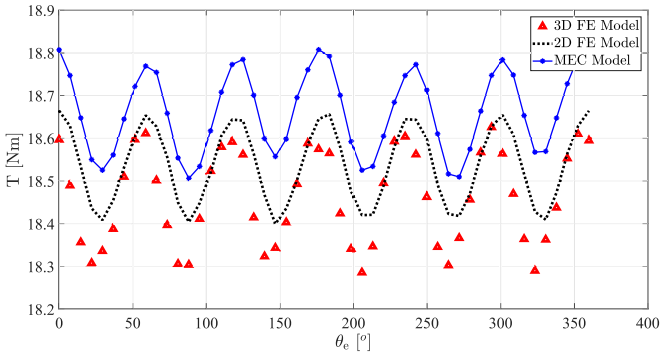

Fig. 9. Torque profile for different models at rated loading condition.

D. Flux Density and Loss Distribution Comparisons

The flux density distribution at the rated loading condition between the 3D FE, 2D FE and MEC models at a certain position are shown in Figs. 12 (a), (b) and (c) respectively. The labels (R, θ_m, y) depict the cylindrical co-ordinates shown in Figs. 2 (b) and (c). For the 2D FE and the MEC models, the flux density in each point (x, y in Fig. 2 (c)) of the plane is averaged over the number of slices taken. In the MEC model, there are some space in the figure at the end of the teeth and in the rotor. This is due to the computation of the flux densities in grid points. In each grid point the flux is assumed to be constant.

In conclusions, in addition to the accurate computations of voltages and torque shown in previous figures, the conclusion from Figs. 12 (a), (b) and (c) is that the MEC achieves accurate flux density prediction in all points in the stator, airgap and rotor.

The iron loss distribution inside the teeth in [W/m^3] at

TABLE III
MEAN VALUES FOR THE TORQUE FOR DIFFERENT LOADING AND GEOMETRICAL CONDITIONS.

b_{so}	I	Parameter	3D FE Model	2D FE Model	MEC Model
3mm	I_{rated}	T_{mean} [Nm]	18.46	18.54	18.66
		$\text{Error}_{T_{\text{mean}}}$ [%]	-	0.43	1.1
		$T_{\text{p-p}}$ [Nm]	0.34	0.26	0.30
		$T_{\text{p-p}_{\text{Model}}}/T_{\text{mean}_{\text{3DFE}}}$ [%]	1.8	1.4	1.6
7mm	I_{rated}	T_{mean} [Nm]	17.96	18.11	18.14
		$\text{Error}_{T_{\text{mean}}}$ [%]	-	0.84	1
		$T_{\text{p-p}}$ [Nm]	0.19	0.16	0.23
		$T_{\text{p-p}_{\text{Model}}}/T_{\text{mean}_{\text{3DFE}}}$ [%]	1.1	0.9	1.3

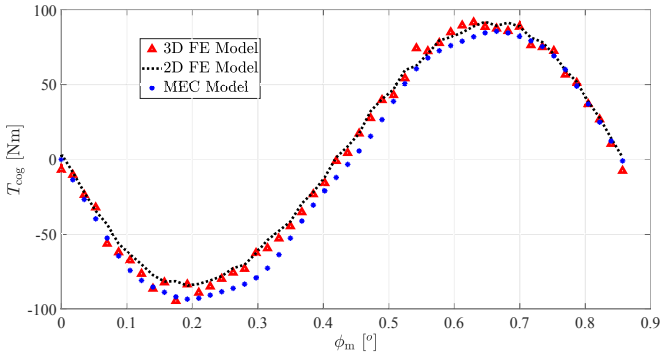

Fig. 10. Cogging torque profile for different models as a function of the rotor position in mechanical degrees.

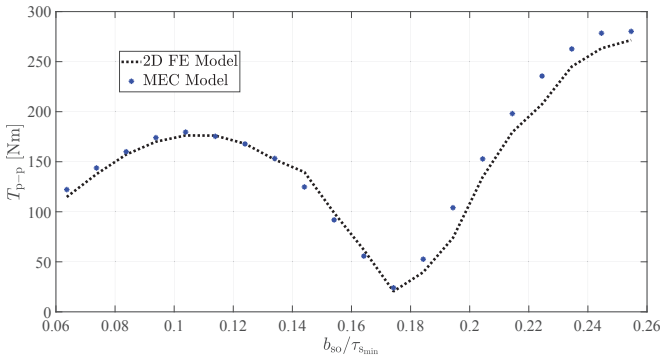

Fig. 11. Cogging torque response as a function of the slot opening.

rated loading condition between the 3D FE, 2D FE and MEC models are shown in Figs. 13 (a), (b) and (c) respectively. The loss distribution for the 2D FE and the MEC models are averaged over the number of slices taken. As a conclusion from these figures, the MEC model can accurately predict the loss distribution of the AFPMSM machine.

Table IV summarizes the stator core iron losses inside the machine. It shows that the MEC model can accurately predict the total iron losses accurately. The comparison is done for different loading and geometrical conditions. The maximum difference compared to the 3D FE model is 6%.

E. CPU Time Comparison

Table V summarizes the CPU time for each of the tested models. All calculations are done on a PC operating a 64-bit

TABLE IV
STATOR IRON LOSSES COMPARISON FOR DIFFERENT LOADING AND GEOMETRICAL CONDITIONS.

b_{so}	I	Parameter	3D FE Model	2D FE Model	MEC Model
3mm	0	P_{iron} [W]	181.7	188	188.8
		$Error_{P_{iron}}$ [%]	-	3.5	3.9
	I_{rated}	P_{iron} [W]	201.4	200.8	202
		$Error_{P_{iron}}$ [%]	-	0.3	0.7
7mm	0	P_{iron} [W]	162.7	170.6	172.3
		$Error_{P_{iron}}$ [%]	-	4.9	5.8
	I_{rated}	P_{iron} [W]	175.6	177.1	179
		$Error_{P_{iron}}$ [%]	-	0.85	1.9

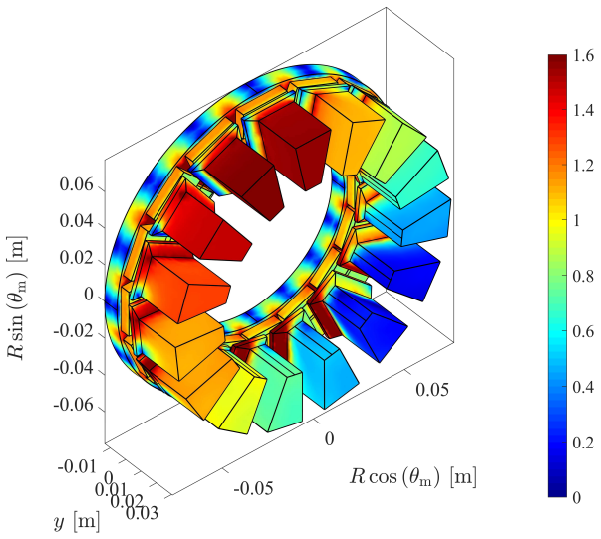

(a) 3D FE Model flux density distribution.

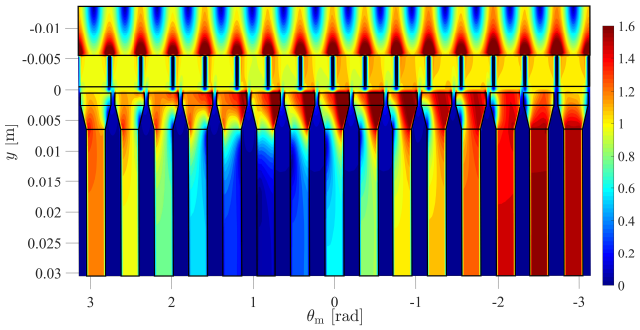

(b) 2D FE model average flux density distribution for different radial slices.

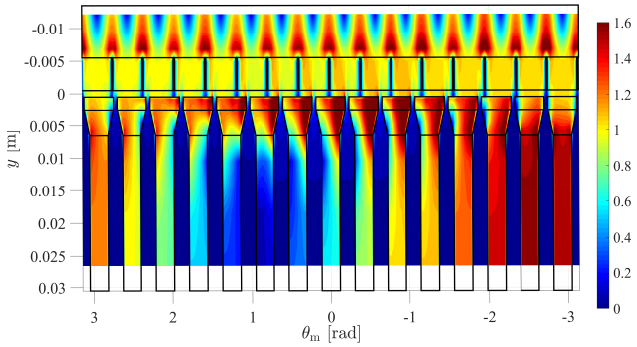

(c) MEC model average flux density distribution for different radial slices.

Fig. 12. Flux density distribution in T for different models at rated loading conditions.

version of Windows 7, the PC has a core i7 processor, and a memory of 16 GB. Both the 2D FE and MEC model divide the machine in six slices. All models were computed for 50 positions of the rotor, equally divided over one cycle. Comsol 3.5 software is used to model the 2D and Comsol 5.3a for the 3D FE models. The 3D FE model has a 100000 tetrahedral with a quadratic shape functions. In the 2D FE model, 8000 triangles are used with quadratic shape function are used to model the machine.

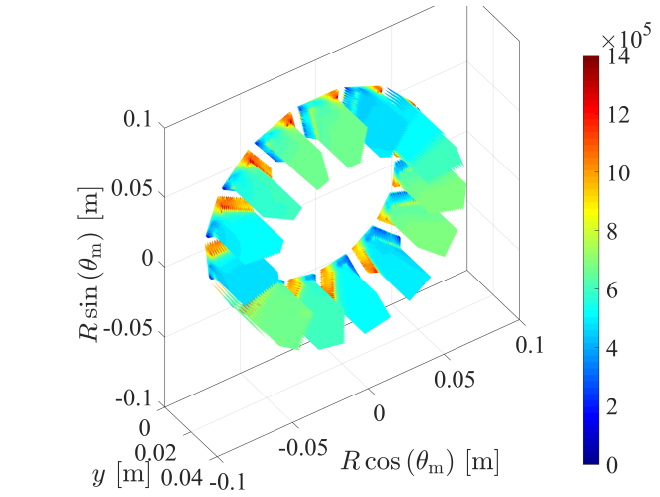

(a) 3D FE Model volumetric iron loss density distribution.

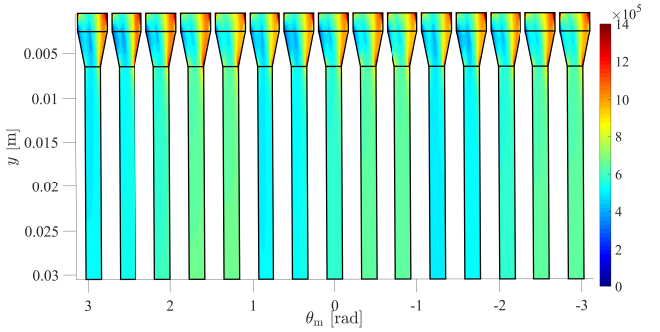

(b) 2D FE Model volumetric iron loss density distribution averaged over number of radial slices taken.

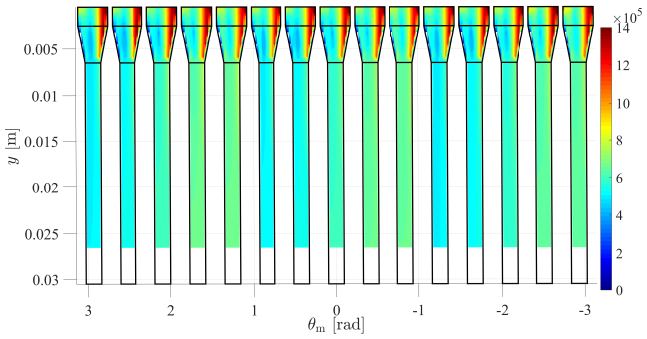

(c) MEC model volumetric iron loss density distribution averaged over number of radial slices taken.

Fig. 13. Volumetric iron loss density distribution in W/m^3 for different models at rated loading conditions.

The comparison is done with a linear and a non-linear permeability. For the non-linear case, the comparison shows that the 3D FE model is very time consuming compared to the other models. The comparison also shows the superiority of the MEC model compared to the FE models. The MEC model takes 55 secs with the non-linear permeability. This is about 900 times faster than the 3D FE model and 600 times faster than the 2D FE model.

For the linear case, all time steps can be computed at once. This reduces the computational time to only 1.5 secs. This is very superior to the information that can be obtained within 1 second regarding the flux density distributions, terminal voltage and torque profile.

TABLE V
COMPARISON OF THE CPU TIME BETWEEN THE FE AND MEC MODELS.

Model Type		CPU Time
Non-Linear models	3D FE Model	15 hrs
	2D FE Model	5.5 hrs
	MEC Model	55 s
Linear models	3D FE Model	10 hrs
	2D FE Model	1 hrs
	MEC Model	1.8 s

F. MEC Model Parameters Optimization and Comparative Study With Conventional MEC

In the developed MEC, the circumferential discretization ($n_{\mathrm{x}} = n_{\mathrm{x1}} = n_{\mathrm{x2}} = n_{\mathrm{x3}}$) and the axial discretization ($n_{\mathrm{y}} = n_{\mathrm{y1}} = n_{\mathrm{y2}} = n_{\mathrm{y3}} = n_{\mathrm{y4}} = n_{\mathrm{y5}} = n_{\mathrm{y6}}$) shown in Fig. 4 can be optimized to keep a good balance between the CPU time and the accuracy of the electromagnetic parameters with respect to the 3D FE model.

Therefore, Fig. 14 shows the effect of n_{x} variations on the percentage errors of the MEC rms voltages V_{MEC}, mean torque $T_{\mathrm{mean_{MEC}}}$, torque ripple $T_{\mathrm{p-p_{MEC}}}$, and iron losses $P_{\mathrm{iron_{MEC}}}$ compared to the 3D FE model rms voltages V_{3DFE}, mean torque $T_{\mathrm{mean_{3DFE}}}$, torque ripple $T_{\mathrm{p-p_{3DFE}}}$, and iron losses $P_{\mathrm{iron_{3DFE}}}$ respectively. The n_{x} is varied in steps from 1 till 8 and the CPU time is noticed for each discretization. In this case n_{y} equals to 3. This test is performed at rated current and a slot opening of 3mm.

To achieve a percentage error of less than 5% for all electromagnetic parameters, a minimum choice of two discretization in the circumferential direction n_{x} is mandatory. In this case, the CPU time is reduced to 10s. The same test is done for different geometrical and loading conditions and the same conclusions are obtained.

Moreover, n_{y} plays an important role in the accuracy of the results and the CPU time. Therefore, the percentage errors of all electromagnetic parameters described before are noticed with respect to the variations of n_{y}. n_{x} is fixed at 2 in this case. The results of this experiment can be noted from Fig. 15. A choice of 2 axial discretization n_{y} would keep the error below 5% for all electromagnetic parameters. The CPU time in this case is reduced to 5.4s.

In addition, the change of radial slices n_{s}, noted in Fig. 2 (b), affects the results accuracy and the CPU time. Therefore, the number of slices is varied from 2 till 8 with a step of 2. The circumferential n_{x} and axial n_{y} discretization are kept to be 2 and 2 respectively. Fig. 16 shows the variation of the percentage error of the electromagnetic parameters with respect to n_{s}. It shows that an optimum selection of 4 radial slices keeps the error within 5%. The CPU time is reduced to 3.2s. It is clear from the above optimizations that an accuracy of the electromagnetic parameters of 5% can be achievable with a CPU time of only 3.2s including the non-linear behavior

TABLE VI
RMS VALUES FOR THE VOLTAGE AND TORQUE PROFILE FOR RATED LOADING CURRENT AND 3MM SLOT OPENING COMPARISON BETWEEN THE 3D FE MODEL, CONVENTIONAL MEC MODEL, AND THE NEW MEC MODEL.

Parameter	3D FE Model	Conventional MEC Model	New MEC Model
V_{rms} [V]	247	277.6	244
$\mathrm{Error}_{V_{\mathrm{rms}}}$ [%]	-	12.4	1.2
T_{mean} [Nm]	18.46	21.1	19.36
$\mathrm{Error}_{T_{\mathrm{mean}}}$ [%]	-	14.3	4.9
$T_{\mathrm{p-p}}$ [Nm]	0.34	2.24	0.43
$T_{\mathrm{p-p_{Model}}}/T_{\mathrm{mean_{3DFE}}}$ [%]	1.8	12.1	2.3
CPU Time	15hrs	2.7s	3.2s

of the electromagnetic material. In addition, to make a better assessment of the developed MEC model, a comparison with the conventional one is done. The conventional MEC is based on the inter connection between stator and rotor reluctances as shown in Fig. 17. For each rotor position, the air gap reluctance between tooth j and PM k depicted as $R_{\mathrm{j,k}}$ has to be recalculated according to the window function of the tooth and the PM described in [21], [29]. This poses some error, delay, and complexity in the matrices construction for each rotor position. However, in the new developed MEC presented in this article, there is no need to interconnect any rotor or stator relcuctances together. The only moving element is the MMF sources of the PMs.

Table VI summarizes the percentage error in voltage and torque between the 3D FE, conventional MEC and the new MEC models. It also shows the CPU time between both models. The discretization used in the new MEC are the optimized ones (n_{x}=2, n_{y}=2, and n_{s}=4). Table VI depicts that the conventional MEC can predict the electromagnetic parameters with a maximum percentage error of 14.3% in all parameters within a CPU time of 2.7s. While, the new MEC can predict the same electromagnetic parameters with a maximum percentage error of 4.9% in almost the same CPU time. In addition, the model does not need to rearrange the reluctance in the airgap while running the dynamic simulation, which is very suitable for surface PM machines, neither radial flux or axial flux machine.

This shows the high accuracy of the results obtained from the developed MEC model compared to the conventional one within the same CPU time.

In addition, to make a fair comparison with the conventional MEC model, only one radial slice is taken into account in the new MEC model. The model only takes one sec to obtain the solution. The rms value of the phase voltage equals to 252V with a percentage error with the 3D FE model of 2%. In addition, the mean torque output equals 19.9Nm with a percentage error of 7.8%. The torque ripple output is 1Nm. This results in a percentage error to the mean torque of the 3D FE model of 5.7%. This proves out that even if one radial slice is considered, the result is still better than the conventional MEC approach. However, many authors use complex PM shapes [30] to reduce the torque ripple and cogging torque. In this case additional radial slices are required.

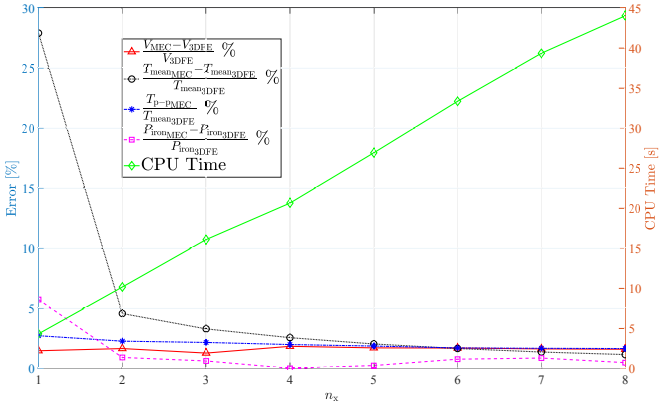

Fig. 14. The percentage error of the machine electromagnetic parameters (Voltage, mean torque, ripple torque, and iron losses) of the MEC model compared to the 3D FE model results on the left scale. The CPU time is on the right scale. The horizontal axis represents the circumferential discretization.

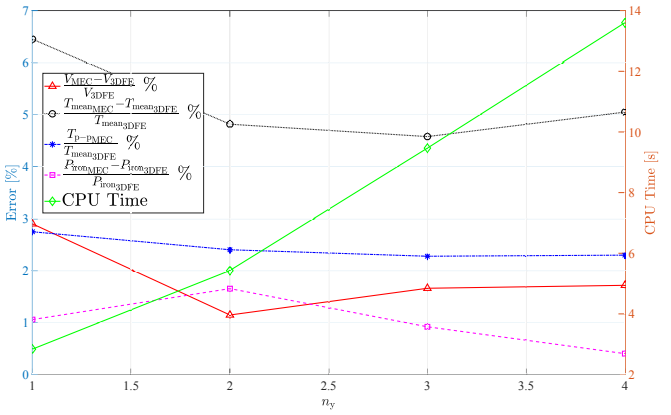

Fig. 15. The percentage error of the machine electromagnetic parameters (Voltage, mean torque, ripple torque, and iron losses) of the MEC model compared to the 3D FE model results on the left scale. The CPU time is on the right scale. The horizontal axis represents the axial discretization.

IV. EXPERIMENTAL VALIDATIONS

The stator core of the YASA machine consists of thin laminated grain oriented material. The lamination thickness is 0.23mm. The iron losses coefficients for the GO material $k_{\mathrm{Fe,1}}$-$k_{\mathrm{Fe,6}}$ described in (15) are 7.4e-3, 2, 1.02686e-06, 1.407179e-02, 8.35812e-05 respectively. Here, $k_{\mathrm{Fe,1}}$-$k_{\mathrm{Fe,6}}$ are fitted based on quasi-static measurements on an Epstein frame. The excess loss coefficient is fitted based on measured hysteresis loops with amplitudes up to 1.8 T and frequencies between 10Hz and 700 Hz, causing a good correspondence of predicted and measured losses up to frequencies above the rated operating frequency of the motor 333 Hz. The values for The fitted parameters H_0, B_0 and N_{u} for the $\nu_{\mathrm{r}}(B)$ curve described in (12) are 41.4A/m, 1.6T, and 33.2 respectively. The MEC model is adjusted to these parameters while performing the experimental analysis. The windings are placed around the stator core. A plastic end plate is placed between the end-winding and the stator core. A stator housing is made of laminated aluminum sheets to reduce the eddy currents

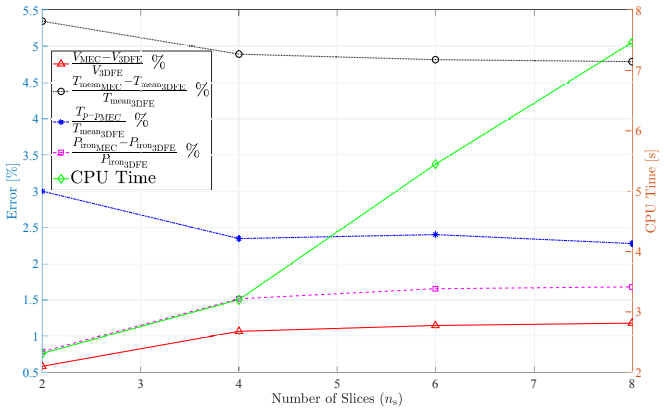

Fig. 16. The percentage error of the machine electromagnetic parameters (Voltage, mean torque, ripple torque, and iron losses) of the MEC model compared to the 3D FE model results on the left scale. The CPU time is on the right scale. The horizontal axis represents the radial number of slices n_s.

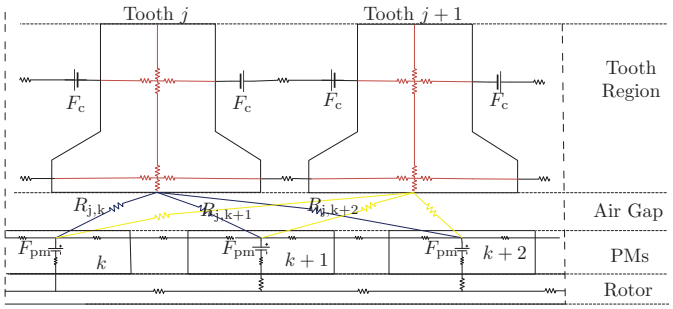

Fig. 17. The conventional MEC sub-division principle.

induced in them. Epoxy potting is used to get the different stator parts bonded into a single solid stator structure.

To perform measurements, the AFPMSM prototype is placed into a test set-up of which an overview is given in Fig. 18. In this test set-up, an asynchronous 7.5 kW, 3000 rpm motor is used as a prime-mover and is powered by a commercial drive. Set-points to this drive for the speed (or torque) are given by a dSPACE 1104 platform. The AFPMSM is used as a generator connected to the fully-programmable three-phase load.

A. Terminal Voltage and Torque Comparisons

The experiment is done at a speed of 2000 rpm. The load of the AFPMSM is a resistive load of 10Ω. The output rms current of the AFPMSM is 9.95A which corresponds to an electromagnetic torque of 14.9Nm. The no load rms voltage is 127.5V. The output full load rms voltage is 101.2V.

Figure 19 shows good agreements between the MEC model and experimental results for the no load and the full load phase voltage. In addition, rms values for the voltage comparisons between the MEC and the experimental results are compared in Table VII. It shows a maximum error of 5.1% between both results.

TABLE VII
RMS PHASE VOLTAGE COMPARISON BETWEEN MEC MODEL AND EXPERIMENTAL RESULTS.

I	Experiment [V]	MEC Model [V]	Error [%]
No Load (I = 0)	127.5	128	0.4
Full Load (I = 9.95A)	101.2	106.4	5.1

For sake of validations, the load resistances are varied experimentally over a wide range from 10Ω till 200Ω. The terminal rms voltages, currents and the output from the torque transducer are measured. The d and q axis currents (I_d, I_q) inputs to the MEC model are adjusted according to the no load voltage measurements, AFPMSM inductance, AFPMSM resistance and load resistance. The d and q axis currents are determined by:

$$I_q + jI_d = \sqrt{2}V_{2000}\frac{n_m}{2000}\frac{1}{((R_l + R_m) + j2\pi f L_m)}, \quad (16)$$

where $V_{n_m=2000}$ is the no load voltage (The electromotive force (EMF)) measurement at 2000rpm which equals 127.5V denoted in Table VII. n_m is the rotational speed in rpm. R_l, R_m are the load and motor resistances respectively. The motor resistance equals 0.27Ω. f is the operating frequency in Hz. L_m is the motor inductance which equals 4.3mH.

Figure 20 shows the difference between the experimental setup measurements and the MEC model results for the rms terminal voltage at two different speeds of 1000rpm and 2000rpm. Due to the resistive load, the machine operates with a negative d axis current. A smaller resistance (larger current) leads to a reduced voltage which is known by the field weakening operation. The figure shows that the MEC model gives higher amplitudes than the experimental setup. This is a consequence of the lesser inductance anticipated by the model.

However, Fig. 21 shows the percentage error between the experiments and the MEC model for the two different speeds for the terminal voltage. It shows that the maximum percentage error is about 5% from the experimental measurements.

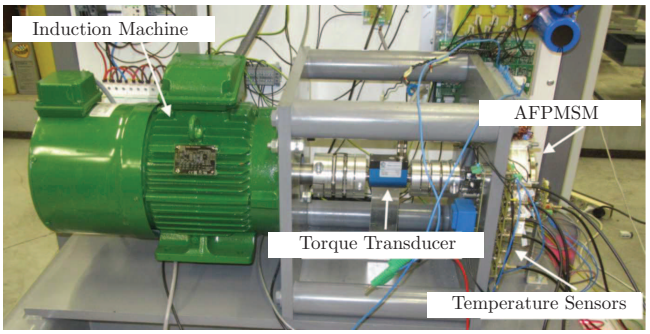

Fig. 18. Axial-flux PM machine test set-up. From left to right: load (asynchronous) machine, torque sensor with couplings, axial flux PM prototype machine.

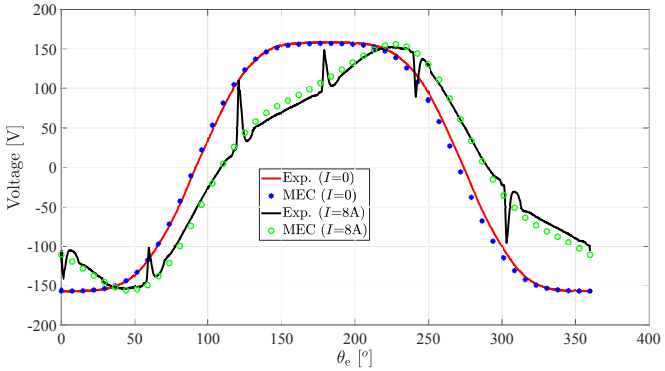

Fig. 19. Comparison of no load and full load phase voltages for the experiment and the MEC model.

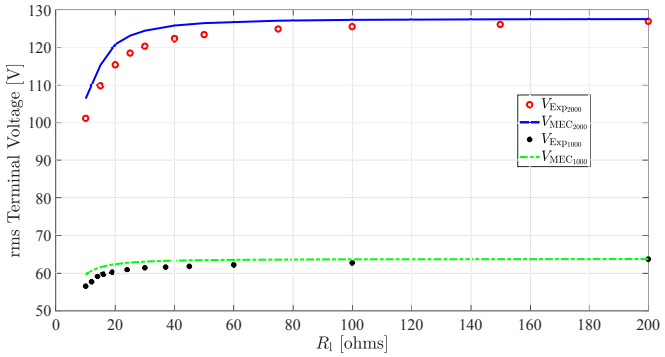

Fig. 20. The rms terminal voltages for different load resistances (R_l) at two different speeds (1000rpm and 2000rpm) for the experiment and the MEC model.

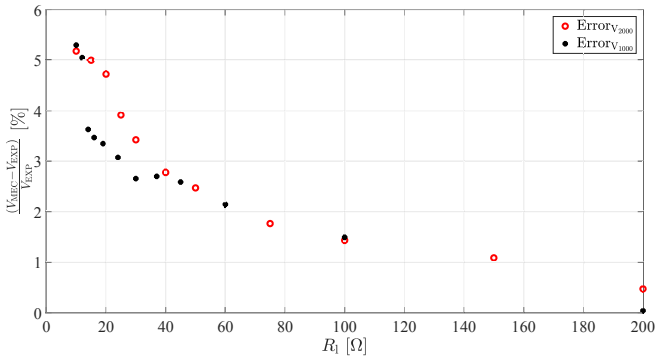

Fig. 21. Percentage error difference between the experiment and the MEC model for the rms terminal voltages for different load resistances (R_l) at two different speeds (1000rpm and 2000rpm).

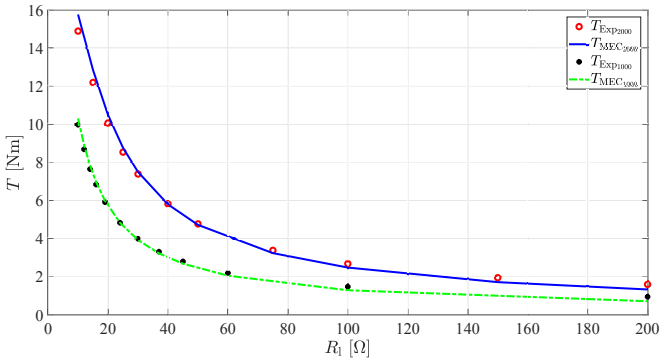

Fig. 22. The torque for different load resistances (R_l) at two different speeds (1000rpm and 2000rpm) for the experiment and the MEC model.

Figure 22 shows the difference between the experimental setup measurements and the MEC model results for the input torque at two different speeds of 1000rpm and 2000rpm. The figure shows clearly that the MEC model can easily track the same response as the experimental setup.

Figure 23 depicts the percentage error between the experiments and the MEC model. It shows that the maximum percentage error is about 5% from the experimental measurements at high loads (low load resistance). However, at lower loads, the percentage error increases to 25%. This is a consequence of the increased effect of the bearing and windage losses at low loads. Therefore, noticeable difference would be observed at low loads.

B. Loss Comparison

The iron loss presents a major part of the total losses of the YASA machine. Therefore, it is mandatory to verify the robustness of the MEC model with respect to the losses. However, it is a difficult task to segregate the iron losses from the total measured losses. Therefore, a similar inverse thermal modeling to [31], [32] is used.

The method used is based on the least square nonlinear (MATLAB function lsqnonlin) fitting method. The inputs to the models are the experimental measured temperatures for the winding, core and rotor. The outputs are the winding, core, and rotor losses. The thermal models used were presented in [33], [34]. They are based on 3D FE and lumped parameter thermal networks (LPTN) for the machine. The convection coefficients used are based on computational fluid dynamics analysis. These models were experimentally validated.

The thermal experiment is conducted at no load and 10Ω load resistance at 2000rpm. The lsqnonlin tries to fit the loss components to obtain the same experimental temperatures. Figs. 24 and 25 show the thermal FE winding, core and PM temperatures with the experimental ones at no load and 10Ω load resistance respectively. They show that the thermal models are capable to track the same response as the experimental setup.

Figures 26 (a), (b) show the temperature distributions for rotor and the PMs at steady state at no load and the 10Ω load resistance. In addition, Figures 26 (c), (d) are depicted for the stator. Table VIII depicts the core, winding and rotor losses from the output of the lsqnonlin and the MEC model at the studied loading conditions. The table shows that the MEC model is capable of predicting the iron losses with a maximum percentage error of 26.34%.

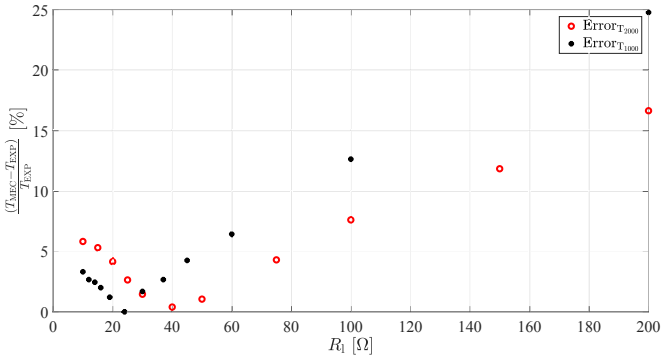

Fig. 23. Percentage error difference between the experiment and the MEC model for the torque for different load resistances (R_l) at two different speeds (1000rpm and 2000rpm).

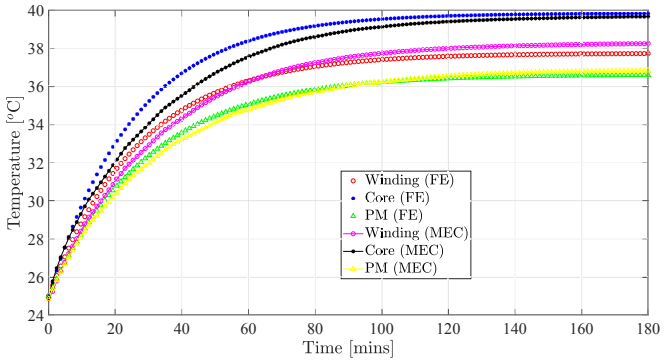

Fig. 24. Winding, core, and PM temperature in (^{o}C) for the experimental and FE model at no load at 2000rpm.

V. Conclusions

This paper presents a fast and a simple semi analytical model based on magnetic equivalent circuit (MEC) model for axial flux permanent magnet synchronous machines (AF-PMSM). This model can be extended for all surface permanent magnet machines. The main novelty of the model is the static reluctance network elements despite rotation. The permanent magnets (PMs) are modeled by an equivalent Fourier series based model. This Fourier series is a time dependent. This simplifies the region of the PMs to only time dependent sources with fixed reluctances. Consequently, the stator, air gap, PM, and rotor reluctances are kept constant in all time steps. This boosts the simulation time and simplifies the solution in the linear case and simplifies the solution in the non-linear case. Moreover, to account for the 3D effect, a multi-slicing in the radial direction is done. On each radial slice, the solution is computed individually. All radial slices are computed within the same matrix.

The performance of the MEC model is validated at several loading and geometrical conditions. The model is compared with 3D and 2D multi-slicing FE models. The comparisons show a maximum error deviation of 1.8%, 1.1%, 1.6%, 6% for the rms value of the voltage, the mean torque, the torque ripple, and the loss computations. Moreover, the iron loss distributions in the MEC are compared with both FE models.

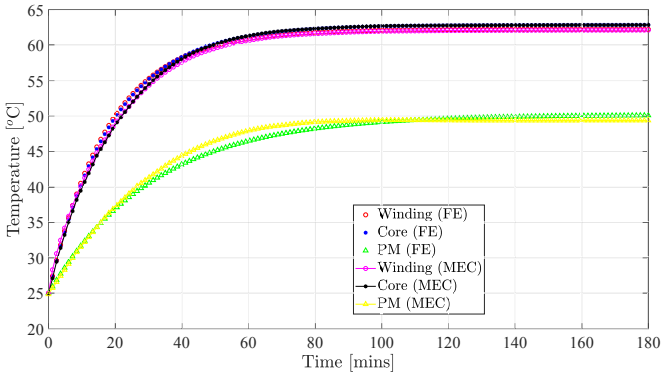

Fig. 25. Winding, core, and PM temperature in (^{o}C) for the experimental and FE model at 10Ω load resistance at 2000rpm.

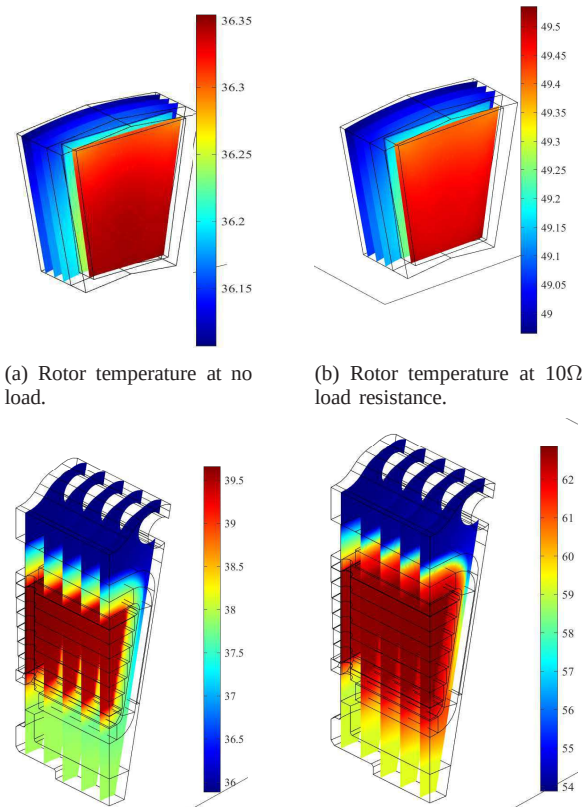

(a) Rotor temperature at no load.

(b) Rotor temperature at 10Ω load resistance.

(c) Stator temperature at no load.

(d) Stator temperature at 10Ω load resistance.

Fig. 26. Temperature distribution of the rotor and stator in (^{o}C) at no load and 10Ω load resistance at 2000rpm for the FE model.

The comparisons show the superiority of the MEC model. The cogging torque for different geometrical parameters is compared with the FE models. A distinguished performance of the MEC model is observed in terms of computation time versus accuracy. Although, sinusoidal current supply is used in this case, the model can work directly with different current waveforms depending on the supply type. The ability of the post-processing loss models to predict the losses at distorted flux waveforms depends on the applied loss model. This is valid also for FE solvers also, if a post-processing model is

TABLE VIII
LOSS DIFFERENCE BETWEEN THE EXPERIMENTAL SETUP AND THE MEC MODEL.

Load type	Loss type	Experimental Setup	MEC model	Error [%]
No Load (I = 0)	Core Losses (W)	25.1	19	24.3%
	Winding Losses (W)	0	-	-
	Rotor Losses (W)	7.5	-	-
$R_{\rm l}$=10Ω	Core Losses (W)	20.5	15.1	26.34%
	Winding Losses (W)	80	-	-
	Rotor Losses (W)	10	-	-

used.

Regarding the simulation time, the MEC model only takes about 1.5 seconds with a constant permeability for 6 radial slices and 50 time steps. In the non-linear case, it takes 55 seconds. In non-linear case, it is 900 times faster than the 3D FE model and 600 times faster than the 2D FE model. Lastly, the model is verified by a 4kW AFPMSM test setup. The MEC model proves also a very good performance in comparison with the experimental setup results. In conclusions, the MEC model can be used to obtain all the electromagnetic parameters of the machine for different geometrical and loading conditions.

APPENDIX

Figure 27 shows an example of a simple reluctance network. This network is provided to give a better understanding of how to use the equations (7)-(11).

This network consists of a magnetomotive-force source E in [A.turns] and three reluctances $R_{1\rm b}$,$R_{2\rm b}$,$R_{3\rm b}$. These reluctances are multiplied afterwards by the relative non-linear reluctivity of $\nu_{\rm r}(B_{1\rm b})$, $\nu_{\rm r}(B_{2\rm b})$, $\nu_{\rm r}(B_{3\rm b})$ that are dependent on each branch flux densities $B_{1\rm b}$, $B_{2\rm b}$, and $B_{3\rm b}$ in [T] respectively. There are two flux loops $\Phi_{1\rm l}$, and $\Phi_{2\rm l}$ and three branch fluxes $\Phi_{1\rm b}$, $\Phi_{2\rm b}$, and $\Phi_{3\rm b}$ to be solved using the Newton-Raphson approach described in (7)-(11).

In this example, the number of loops $n_{\rm l} = 2$ and the number of branches $n_{\rm b} = 3$. The magnetomotive-force vector $\mathbf{F}_{\rm c}$ in [A.turns], the diagonal reluctance matrix $\mathbf{R}_{\rm d}$ in [A.turns/Wb], the loop flux $\mathbf{\Phi}$ in [Wb], the relative reluctivity matrix $\nu_{\rm r}$, and the loop matrix $\mathbf{L}$ described in (8) can be described as:

$$\mathbf{F}_{\rm c} = \begin{bmatrix} E \\ 0 \end{bmatrix}, \quad \mathbf{R}_{\rm d} = \begin{bmatrix} R_{1\rm b} & 0 & 0 \\ 0 & R_{2\rm b} & 0 \\ 0 & 0 & R_{3\rm b} \end{bmatrix}, \quad \mathbf{\Phi} = \begin{bmatrix} \Phi_{1\rm l} \\ \Phi_{2\rm l} \end{bmatrix},$$
$$\nu_{\rm r} = \begin{bmatrix} \nu_{\rm r}(B_{1\rm b}) & 0 & 0 \\ 0 & \nu_{\rm r}(B_{2\rm b}) & 0 \\ 0 & 0 & \nu_{\rm r}(B_{3\rm b}) \end{bmatrix}, \quad \mathbf{L} = \begin{bmatrix} 1 & 0 \\ 1 & -1 \\ 0 & 1 \end{bmatrix}, \tag{17}$$

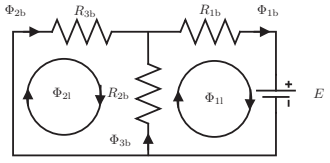

Fig. 27. A simple reluctance network.

where $B_{1\rm b}$, $B_{2\rm b}$, $B_{3\rm b}$ are the flux densities for each branch.

The residual function $\mathbf{r}$ in this case equals:

$$\begin{aligned} \mathbf{r} &= \mathbf{L^T}\left(\mathbf{R}_{\rm d} \bullet \nu_{\rm r}\right)\mathbf{L}\mathbf{\Phi} - \mathbf{F}_{\rm c} = \mathbf{R}\mathbf{\Phi} - \mathbf{F}_{\rm c} \\ &= \begin{bmatrix} R_{1\rm b}\nu_{\rm r}(B_{1\rm b}) + R_{2\rm b}\nu_{\rm r}(B_{2\rm b}) & -R_{2\rm b}\nu_{\rm r}(B_{2\rm b}) \\ -R_{2\rm b}\nu_{\rm r}(B_{2\rm b}) & R_{3\rm b}\nu_{\rm r}(B_{3\rm b}) + R_{2\rm b}\nu_{\rm r}(B_{2\rm b}) \end{bmatrix} \\ &\quad \begin{bmatrix} \Phi_{1\rm l} \\ \Phi_{2\rm l} \end{bmatrix} - \begin{bmatrix} E \\ 0 \end{bmatrix}, \end{aligned} \tag{18}$$

where the reluctance matrix $\mathbf{R}$ equals $\mathbf{L^T}\left(\mathbf{R}_{\rm d} \bullet \nu_{\rm r}\right)\mathbf{L}$.

To obtain the Jacobian matrix in (10), the matrices $\mathbf{A}_{\rm area}$ in [1/m^2], $\mathbf{U}$, $\nu_{\rm r_{der}}$, and $\mathbf{\Phi}_{\rm d}$ in [Wb] described in (10) need to be evaluated.

$$\mathbf{A}_{\rm area} = \begin{bmatrix} \frac{1}{A_{1\rm b}} & 0 & 0 \\ 0 & \frac{1}{A_{2\rm b}} & 0 \\ 0 & 0 & \frac{1}{A_{3\rm b}} \end{bmatrix}, \quad \mathbf{U} = \begin{bmatrix} 1 & 1 \\ 1 & 1 \end{bmatrix},$$
$$\nu_{\rm r_{der}} = \begin{bmatrix} \nu_{\rm r1_{der}} & 0 & 0 \\ 0 & \nu_{\rm r2_{der}} & 0 \\ 0 & 0 & \nu_{\rm r3_{der}} \end{bmatrix}, \quad \mathbf{\Phi}_{\rm d} = \begin{bmatrix} \Phi_{1\rm l} & 0 \\ 0 & \Phi_{2\rm l} \end{bmatrix}, \tag{19}$$

where $A_{1\rm b}$, $A_{2\rm b}$, $A_{3\rm b}$ are the areas of each branch. $\nu_{\rm r1_{der}} = \frac{\partial \nu_{\rm r}(B_{1\rm b})}{\partial B_{1\rm b}}$ is the first derivative of the relative reluctivity (12) with respect to the flux density at a value of $B_{1\rm b}$. Besides, $\nu_{\rm r2_{der}}$, $\nu_{\rm r3_{der}}$ can be defined similarly.

By substituting the matrices described in (17) and (19) into (10), the Jacobian matrix is obtained.

$$\mathbf{J} = \mathbf{R} + \mathbf{L^T}\begin{bmatrix} \frac{R_{1\rm b}\nu_{\rm r1_{der}}}{A_{1\rm b}} & 0 & 0 \\ 0 & \frac{R_{2\rm b}\nu_{\rm r2_{der}}}{A_{2\rm b}} & 0 \\ 0 & 0 & \frac{R_{3\rm b}\nu_{\rm r3_{der}}}{A_{3\rm b}} \end{bmatrix}\Big(\left(\mathbf{L}\mathbf{\Phi}_{\rm d}\mathbf{U}\right) \bullet \mathbf{L} \Big). \tag{20}$$

The Jacobian matrix equals:

$$\mathbf{J} = \mathbf{R} + \begin{bmatrix} \frac{R_{1\rm b}\nu_{\rm r1_{der}}}{A_{1\rm b}}\Phi_{1\rm l} + \frac{R_{2\rm b}\nu_{\rm r2_{der}}}{A_{2\rm b}}\left(\Phi_{1\rm l} - \Phi_{2\rm l}\right) & -\frac{R_{2\rm b}\nu_{\rm r2_{der}}}{A_{2\rm b}}\left(\Phi_{1\rm l} - \Phi_{2\rm l}\right) \\ -\frac{R_{2\rm b}\nu_{\rm r2_{der}}}{A_{2\rm b}}\left(\Phi_{1\rm l} - \Phi_{2\rm l}\right) & \frac{R_{2\rm b}\nu_{\rm r2_{der}}}{A_{2\rm b}}\left(\Phi_{1\rm l} - \Phi_{2\rm l}\right) + \frac{R_{3\rm b}\nu_{\rm r3_{der}}}{A_{3\rm b}}\Phi_{2\rm l} \end{bmatrix} \tag{21}$$

To obtain the Jacobian matrix $\mathbf{J}$ by the conventional way, it was proven in [20] that $\mathbf{J}$ is divided into two parts. One part is the reluctance matrix term $\mathbf{R}$. The second one describes the change of the reluctance term with respect to the loop flux. Therefore, the first entry of $\mathbf{J}$ can be described as:

$$\begin{aligned} J(1,1) = \frac{\partial r(1,1)}{\partial \Phi_{1\rm l}} &= R(1,1) + \\ &\left(R_{1\rm b}\frac{\partial \nu_{\rm r}(B_{1\rm b})}{\partial \Phi_{1\rm l}} + R_{2\rm b}\frac{\partial \nu_{\rm r}(B_{2\rm b})}{\partial \Phi_{1\rm l}}\right)\Phi_{1\rm l} - \\ &\left(R_{2\rm b}\frac{\partial \nu_{\rm r}(B_{2\rm b})}{\partial \Phi_{1\rm l}}\right)\Phi_{2\rm l}. \end{aligned} \tag{22}$$

The partial derivative term $R_{2\rm b}\frac{\partial \nu_{\rm r}(B_{2\rm b})}{\partial \Phi_{1\rm l}}$ is resolved as follows:

$$R_{2\mathrm{b}}\frac{\partial \nu_{\mathrm{r}}(B_{2\mathrm{b}})}{\partial \Phi_{1\mathrm{l}}} = R_{2\mathrm{b}}\frac{\partial \nu_{\mathrm{r}}(B_{2\mathrm{b}})}{\partial B_{2\mathrm{b}}}\frac{\partial B_{2\mathrm{b}}}{\partial \Phi_{2\mathrm{b}}}\frac{\partial \Phi_{2\mathrm{b}}}{\partial \Phi_{1\mathrm{l}}}, \qquad (23)$$

where $\frac{\partial \nu_{\mathrm{r}}(B_{2\mathrm{b}})}{\partial B_{2\mathrm{b}}} = \nu_{\mathrm{r}2_{\mathrm{der}}}$ can be obtained by differentiating (12) with respect to the flux density at a value of $B_{2\mathrm{b}}$. The term $\frac{\partial B_{2\mathrm{b}}}{\partial \Phi_{2\mathrm{b}}}$ is the inverse of the area ($A_{2\mathrm{b}}$) of this reluctance. $\frac{\partial \Phi_{2\mathrm{b}}}{\partial \Phi_{1\mathrm{l}}}$ denotes the direction of loop flux with respect to the branch flux. If they are on the same direction, it is one. Otherwise, it is -1. This simplifies the solution to:

$$R_{2\mathrm{b}}\frac{\partial \nu_{\mathrm{r}}(B_{2\mathrm{b}})}{\partial \Phi_{1\mathrm{l}}} = R_{2\mathrm{b}}\nu_{\mathrm{r}2_{\mathrm{der}}}\frac{1}{A_{2\mathrm{b}}}1 = \frac{R_{2\mathrm{b}}\nu_{\mathrm{r}2_{\mathrm{der}}}}{A_{2\mathrm{b}}}. \qquad (24)$$

Therefore, the entries of the Jacobian matrix **J** can be obtained as:

$$\begin{aligned}
J(1,1) =& R(1,1) + \left(\frac{R_{1\mathrm{b}}\nu_{\mathrm{r}1_{\mathrm{der}}}}{A_{1\mathrm{b}}} + \frac{R_{2\mathrm{b}}\nu_{\mathrm{r}2_{\mathrm{der}}}}{A_{2\mathrm{b}}}\right)\Phi_{1\mathrm{l}} - \frac{R_{2\mathrm{b}}\nu_{\mathrm{r}2_{\mathrm{der}}}}{A_{2\mathrm{b}}}\Phi_{2\mathrm{l}},\\
J(1,2) =& R(1,2) - \frac{R_{2\mathrm{b}}\nu_{\mathrm{r}2_{\mathrm{der}}}}{A_{2\mathrm{b}}}\Phi_{1\mathrm{l}} + \frac{R_{2\mathrm{b}}\nu_{\mathrm{r}2_{\mathrm{der}}}}{A_{2\mathrm{b}}}\Phi_{2\mathrm{l}},\\
J(2,1) =& R(2,1) - \frac{R_{2\mathrm{b}}\nu_{\mathrm{r}2_{\mathrm{der}}}}{A_{2\mathrm{b}}}\Phi_{1\mathrm{l}} + \frac{R_{2\mathrm{b}}\nu_{\mathrm{r}2_{\mathrm{der}}}}{A_{2\mathrm{b}}}\Phi_{2\mathrm{l}},\\
J(2,2) =& R(2,2) + \frac{R_{2\mathrm{b}}\nu_{\mathrm{r}2_{\mathrm{der}}}}{A_{2\mathrm{b}}}\Phi_{1\mathrm{l}}\\
&+ \left(-\frac{R_{2\mathrm{b}}\nu_{\mathrm{r}2_{\mathrm{der}}}}{A_{2\mathrm{b}}} + \frac{R_{3\mathrm{b}}\nu_{\mathrm{r}3_{\mathrm{der}}}}{A_{3\mathrm{b}}}\right)\Phi_{2\mathrm{l}}.
\end{aligned} \qquad (25)$$

By comparing (21) and (25), the same solution is obtained by the two methods. However, The traditional method of obtaining the Jacobian matrix is a heavy computational task. Therefore, the method described in (10) provides a fast solution for the Jacobian matrix without the need for any for loops. The use of sparse matrices alow the fast computation of the Jacobian matrix.

REFERENCES

[1] A. Hemeida, M. Taha, A. A. E. Abdallh, H. Vansompel, L. Dupré, and P. Sergeant, "Applicability of Fractional Slot Axial Flux Permanent Magnet Synchronous Machines in the Field Weakening Region," *IEEE Transactions on Energy Conversion*, vol. 32, DOI 10.1109/TEC.2016.2614011, no. 1, pp. 111–121, Mar. 2016.

[2] H. Tiegna, Y. Amara, and G. Barakat, "Study of cogging torque in axial flux permanent magnet machines using an analytical model," *IEEE Transactions on Magnetics*, vol. 50, DOI 10.1109/TMAG.2013.2279075, no. 2, pp. 845–848, 2014.

[3] B. Hannon, P. Sergeant, and L. Dupré, "2-D Analytical Subdomain Model of a Slotted PMSM With Shielding Cylinder," *IEEE Transactions on Magnetics*, vol. 50, DOI 10.1109/TMAG.2014.2309325, no. 7, p. 8101410, Jul. 2014.

[4] H. Tiegna, A. Bellara, Y. Amara, and G. Barakat, "Analytical modeling of the open-circuit magnetic field in axial flux permanent-magnet machines with semi-closed slots," *IEEE Transactions on Magnetics*, vol. 48, DOI 10.1109/TMAG.2011.2171979, no. 3, pp. 1212–1226, 2012.

[5] A. Parviainen, M. Niemelä, and J. Pyrhönen, "Modeling of axial flux permanent-magnet machines," *IEEE Transactions on Industry Applications*, vol. 40, DOI 10.1109/TIA.2004.834086, no. 5, pp. 1333–1340, 2004.

[6] H. Vansompel, P. Sergeant, and L. Dupré, "A multilayer 2-D-2-D coupled model for eddy current calculation in the rotor of an axial-flux PM machine," *IEEE Transactions on Energy Conversion*, vol. 27, DOI 10.1109/TEC.2012.2192737, no. 3, pp. 784–791, Sep. 2012.

[7] A. Hemeida, B. Hannon, H. Vansompel, and P. Sergeant, "Comparison of three analytical methods for the precise calculation of cogging torque and torque ripple in axial flux PM machines," *Mathematical Problems in Engineering*, DOI 10.1155/2016/2171547, p. 2171547, 2016.

[8] A. Dwivedi, S. N. Mahendra, R. K. Srivastava, and S. K. Singh, "Comparative study and performance evaluation of analytical methods for surface mounted permanent magnet brushless motors," *IET Power Electronics*, vol. 9, DOI 10.1049/iet-pel.2016.0179, no. 11, pp. 2289–2297, Sep. 2016.

[9] H. Tiegna, Y. Amara, and G. Barakat, "Overview of analytical models of permanent magnet electrical machines for analysis and design purposes," *Mathematics and Computers in Simulation*, vol. 90, DOI 10.1016/j.matcom.2012.12.002, pp. 162–177, 2013.

[10] M. F. Hsieh and Y. C. Hsu, "A generalized magnetic circuit modeling approach for design of surface permanent-magnet machines," *IEEE Transactions on Industrial Electronics*, vol. 59, DOI 10.1109/TIE.2011.2161251, no. 2, pp. 779–792, Feb. 2012.

[11] T. Raminosoa, J. A. Farooq, A. Djerdir, and A. Miraoui, "Reluctance network modeling of surface permanent magnet motor considering iron nonlinearities," *Energy Conversion and Management*, vol. 50, DOI 10.1016/j.enconman.2009.01.012, no. 5, pp. 1356–1361, 2009.

[12] J. Tangudu, T. Jahns, and A. EL-Refaie, "Core loss prediction using magnetic circuit model for fractional-slot concentrated-winding interior permanent magnet machines," *Energy Conversion Congress and Exposition (ECCE), 2010 IEEE*, DOI 10.1109/ECCE.2010.5617873, pp. 1004–1011, Sep. 2010.

[13] Y. Kano, T. Kosaka, and N. Matsui, "A simple nonlinear magnetic analysis for axial-flux permanent-magnet machines," *IEEE Transactions on Industrial Electronics*, vol. 57, DOI 10.1109/TIE.2009.2034685, no. 6, pp. 2124–2133, 2010.

[14] L. J. Wu, Z. Q. Zhu, D. A. Staton, M. Popescu, and D. Hawkins, "Comparison of analytical models of cogging torque in surface-mounted PM machines," *IEEE Transactions on Industrial Electronics*, vol. 59, DOI 10.1109/TIE.2011.2143379, no. 6, pp. 2414–2425, Jun. 2012.

[15] F. Dubas and K. Boughrara, "New Scientific Contribution on the 2-D Subdomain Technique in Polar Coordinates: Taking into Account of Iron Parts," DOI 10.20944/PREPRINTS201708.0052.V1, Aug. 2017.

[16] A. Hemeida and P. Sergeant, "Analytical modeling of surface PMSM using a combined solution of Maxwell's equations and magnetic equivalent circuit," *IEEE Transactions on Magnetics*, vol. 50, DOI 10.1109/TMAG.2014.2330801, no. 12, p. 7027913, 2014.

[17] S. Ouagued, Y. Amara, and G. Barakat, "Comparison of hybrid analytical modelling and reluctance network modeling for pre-design purposes," *Mathematics and Computers in Simulation*, vol. 130, DOI 10.1016/j.matcom.2016.05.001, pp. 3–21, 2016.

[18] H. Tiegna, Y. Amara, and G. Barakat, "Validity domain of a quasi-3D multislice analytical model for synchronous axial flux machines with trapezoidal magnets," *The European Physical Journal Applied Physics*, vol. 70, DOI 10.1051/epjap/2015140495, no. 1, p. 10902, Apr. 2015.

[19] A. Hemeida, P. Sergeant, and H. Vansompel, "Comparison of Methods for Permanent Magnet Eddy Current Loss Computations With and Without Reaction Field Considerations in Axial Flux PMSM," *IEEE Transactions on Magnetics*, vol. 51, DOI 10.1109/TMAG.2015.2431222, no. 9, p. 8107511, 2015.

[20] H. W. Derbas, J. M. Williams, A. C. Koenig, and S. D. Pekarek, "A Comparison of Nodal- and Mesh-Based Magnetic Equivalent Circuit Models," *IEEE Transactions on Energy Conversion*, vol. 24, DOI 10.1109/TEC.2008.2002037, no. 2, pp. 388–396, Jun. 2009.

[21] A. Lehikoinen, S. B. Shah, and A. Arkkio, "Time-Stepping 3d-Reluctance Network Analysis of An Axial Flux Permanent Magnet Machine," in *Proceedings of EPNC 2016*, pp. 67–68, Helsinki, 2016.

[22] A. M. A. Abdallh, "An Inverse Problem Based Methodology with Uncertainty Analysis for the Identification of Magnetic Material Characteristics of Electromagnetic Devices," *PhD dissertation, Ghent University*, 2012.

[23] P. Rasilo, E. Dlala, K. Fonteyn, J. Pippuri, A. Belahcen, and A. Arkkio, "Model of laminated ferromagnetic cores for loss prediction in electrical machines," *IET Electric Power Applications*, vol. 5, DOI 10.1049/iet-epa.2010.0270, no. 7, p. 580, 2011.

[24] A. M. Knight, J. C. Salmon, and J. Ewanchuk, "Integration of a First Order Eddy Current Approximation With 2D FEA for Prediction of PWM Harmonic Losses in Electrical Machines," *IEEE Transactions on Magnetics*, vol. 49, DOI 10.1109/TMAG.2013.2242055, no. 5, pp. 1957–1960, May. 2013.

[25] J. H. J. Potgieter and M. J. Kamper, "Calculation Methods and Effects of End-Winding Inductance and Permanent-Magnet End Flux on Performance Prediction of Nonoverlap Winding Permanent-Magnet Machines," *IEEE Transactions on Industry Applications*, vol. 50, DOI 10.1109/TIA.2013.2295468, no. 4, pp. 2458–2466, Jul. 2014.

[26] G. Bertotti, "General Properties of Power Losses in Soft Ferromagnetic Materials." *IEEE Transactions on Magnetics*, vol. 24, DOI 10.1109/20.43994, no. 1, pp. 621–630, 1987.

[27] E. Barbisio, F. Fiorillo, and C. Ragusa, "Predicting loss in magnetic steels under arbitrary induction waveform and with minor hysteresis loops," *IEEE Transactions on Magnetics*, vol. 40, DOI 10.1109/TMAG.2004.830510, no. 4 I, pp. 1810–1819, 2004.

[28] L. Zhu, S. Z. Jiang, Z. Q. Zhu, and C. C. Chan, "Analytical methods for minimizing cogging torque in permanent-magnet machines," *IEEE Transactions on Magnetics*, vol. 45, DOI 10.1109/TMAG.2008.2011363, no. 4, pp. 2023–2031, Apr. 2009.
[29] G. Sizov, A. Sayed-Ahmed, Chia-Chou Yeh, and N. Demerdash, "Analysis and Diagnostics of Adjacent and Nonadjacent Broken-Rotor-Bar Faults in Squirrel-Cage Induction Machines," *IEEE Transactions on Industrial Electronics*, vol. 56, DOI 10.1109/TIE.2008.2011341, no. 11, pp. 4627–4641, Nov. 2009.
[30] M. Aydin and M. Gulec, "Reduction of cogging torque in double-rotor axial-flux permanent-magnet disk motors: A review of cost-effective magnet-skewing techniques with experimental verification," *IEEE Transactions on Industrial Electronics*, vol. 61, DOI 10.1109/TIE.2013.2276777, no. 9, pp. 5025–5034, Sep. 2014.
[31] D. G. Nair and A. Arkkio, "Inverse Thermal Modeling to Determine Power Losses in Induction Motor," *IEEE Transactions on Magnetics*, vol. 53, DOI 10.1109/TMAG.2017.2661381, no. 6, pp. 1–4, Jun. 2017.
[32] H. Vansompel, A. Yarantseva, P. Sergeant, and G. Crevecoeur, "An Inverse Thermal Modeling Approach for Thermal Parameter and Loss Identification in an Axial Flux Permanent Magnet Machine," *IEEE Transactions on Industrial Electronics*, vol. Early Access, DOI 10.1109/TIE.2018.2838089, 2018.
[33] A. Mohamed, A. Hemeida, A. Rashekh, H. Vansompel, A. Arkkio, and P. Sergeant, "A 3D dynamic lumped parameter thermal network of air-cooled yasa axial flux permanent magnet synchronous machine," *Energies*, vol. 11, DOI 10.3390/en11040774, no. 4, 2018.
[34] H. Vansompel, A. Rasekh, A. Hemeida, J. Vierendeels, and P. Sergeant, "Coupled Electromagnetic and Thermal Analysis of an Axial Flux PM Machine," *IEEE Transactions on Magnetics*, vol. 51, DOI 10.1109/TMAG.2015.2433392, no. 11, p. 8108104, Nov. 2015.

Ahmed Hemeida was born in Egypt in 1987. He received the B.Sc. and M.Sc. degrees from the department of electrical power and engineering, Cairo University, Egypt, in 2009 and 2012, respectively. In 2017, he obtained his Ph.D degree in the Department of Electrical Energy, Metals, Mechanical Constructions and Systems, Ghent University, Belgium. He is currently a Postdoctoral Research Assistant with the department of electrical Engineering in Aalto University in Finland. His research interests include the modeling and design of electrical machines.

Antti Lehikoinen was born in Joensuu, Finland, in 1988. He received the B.Sc. (Tech.), M.Sc. (Tech.), and D.Sc. (Tech.) degrees in electromechanics from the School of Electrical Engineering, Aalto University, Espoo, Finland, in 2012, 2013, and 2017 respectively. Since 2017, he is a post-doc in the Research Group of Electromechanics. His current research interests include development of computationally-efficient numerical winding loss models, the stochastic properties of circulating currents in random-wound electrical machines, as well as minimization of manufacture-related additional losses. He has also the authored the open-source FEA library SMEKlib for Matlab, and collaborated actively with various start-ups and SMEs for the development of novel electromechanical devices.

Paavo Rasilo received his M.Sc. (Tech.) and D.Sc. (Tech.) degrees from Helsinki University of Technology (currently Aalto University) and Aalto University, Espoo, Finland in 2008 and 2012, respectively. He is currently working as an Assistant Professor at the Department of Electrical Engineering, Tampere University of Technology, Tampere, Finland. His research interests deal with numerical modeling of electrical machines as well as power losses and magnetomechanical effects in soft magnetic materials.

Hendrik Vansompel was born in Belgium in 1986. He received the master's and Ph.D. degrees in electromechanical engineering from Ghent University, Ghent, Belgium, in 2009 and 2013, respectively. He is currently a Postdoctoral Research Assistant with the Department of Electrical Energy, Metals, Mechanical Constructions and Systems, Ghent University. His research interests include the design and control of electrical drives.

Anouar Belahcen (M13-SM15) was born in Morocco in 1663. He received the M.Sc. (Tech.) and Doctor (Tech.) degrees from Helsinki University of Technology, Finland, in 1998, and 2004, respectively. He is now Professor of Energy and Power at Aalto University, Finland and Professor of electrical machines at Tallinn University of Technology, Estonia. His research interest are numerical modelling of electrical machines, magnetic materials, coupled magneto-mechanical problems, magnetic forces, magnetostriction, and fault diagnostics of electrical machines.

Antero Arkkio received his M.Sc. (Tech.) and D.Sc. (Tech.) degrees from Helsinki University of Technology in 1980 and 1988. Currently he is a Professor of Electrical Engineering at Aalto University. His research interests deal with modeling, design, and measurement of electrical machines.

Peter Sergeant received the M.Sc. degree in electromechanical engineering and the Ph.D. degree in engineering sciences from Ghent University, Ghent, Belgium, in 2001 and 2006, respectively. In 2001, he became a Researcher with the Electrical Energy Laboratory, Ghent University. He became a Postdoctoral Researcher at Ghent University in 2006 and at Ghent University College in 2008. Since 2012, he has been Associate Professor with Ghent University. His current research interests include numerical methods in combination with optimization techniques to design nonlinear electromagnetic systems, in particular, electrical machines for sustainable energy applications.